



# Joint Survey Processing. II. Stellar Proper Motions in the COSMOS Field from Hubble Space Telescope ACS and Subaru Telescope HSC Observations

Sergio B. Fajardo-Acosta<sup>1</sup> , Andreas Faisst<sup>2</sup> , Carl J. Grillmair<sup>2</sup> , Ranga-Ram Chary<sup>2</sup> , Roberta Paladini<sup>1</sup> , Ben Rusholme<sup>1</sup> , and Nathaniel Stickley<sup>1</sup>

<sup>1</sup> Caltech/IPAC, Mail Code 100-22, Pasadena, CA 91125, USA; [fajardo@ipac.caltech.edu](mailto:fajardo@ipac.caltech.edu)

<sup>2</sup> Caltech/IPAC, Mail Code 314-6, Pasadena, CA 91125, USA

Received 2021 November 20; revised 2022 February 28; accepted 2022 March 1; published 2022 May 4

## Abstract

We analyze stellar proper motions in the COSMOS field to assess the presence of bulk motions. At bright magnitudes ( $G$ -band 18.5–20.76 AB), we use the proper motions of 1010 stars in the Gaia DR2 catalog. At the faint end, we compute proper motions of 11,519 pointlike objects at  $i$ -band magnitudes 19–25 AB using Hubble ACS and Subaru HSC data, which span two epochs about 11 yr apart. In order to measure these proper motions with unprecedented accuracy at faint magnitudes, we developed a foundational set of astrometric tools that will be required for joint survey processing of data from the next generation of optical/infrared surveys. The astrometric grids of Hubble ACS and Subaru HSC mosaics were corrected at the catalog level using proper motion–propagated and parallax-corrected Gaia DR2 sources. These astrometric corrections were verified using compact extragalactic sources. Upon comparison of our measured proper motions with Gaia DR2, we estimate the uncertainties in our measurements to be  $\sim 2\text{--}3 \text{ mas yr}^{-1} \text{ axis}^{-1}$ , down to 25.5 AB mag. We correct proper motions for the mean motion of the Sun, and we find that late-type main-sequence stars predominantly in the thin disk in the COSMOS field have space velocities mainly toward the Galactic center. We detect candidate high-velocity ( $\geq 220 \text{ km s}^{-1}$ ) stars, six of them at  $\sim 0.4\text{--}6 \text{ kpc}$ , from the Gaia sample, and five of them at  $\sim 20 \text{ kpc}$ , from the faint star HSC and ACS sample. The sources from the faint star sample may be candidate halo members of the Sangarius stream.

*Unified Astronomy Thesaurus concepts:* Galaxy structure (622); Galaxy stellar halos (598); Proper motions (1295); Astrometry (80); Catalogs (205); Stellar streams (2166)

## 1. Introduction

The combined analysis of multiwavelength, multimission data sets with different spatial resolutions and time baselines at the pixel level can be a powerful way to uncover phenomenology not discernible with a single data set. It requires astrometry and photometry to be made concordant with high precision, which is sometimes a challenge given the role of source confusion at faint magnitudes, varying point spread functions (PSFs), and different pixel scales. The *joint survey processing* (JSP) effort will, as its name implies, undertake joint pixel-level processing of data from Euclid, the Nancy Grace Roman Space Telescope (formerly known as the Wide-Field Infrared Space Telescope, or WFIRST), and the Vera C. Rubin Observatory (formerly known as the Large Synoptic Survey Telescope, or LSST, an acronym now reserved for the Rubin Observatory’s Legacy Survey of Space and Time; Ivezić et al. 2019). The spatial resolution of the space-platform surveys and their near-infrared bandpasses will enable one to distinguish stars from galaxies while alleviating both source confusion and the role of dust extinction. In comparison, the multivisit cadence of LSST and its  $>10 \text{ yr}$  time baseline, as well as its differential time baseline with the single-visit space surveys, will allow one to study the proper motions of these stars. Measuring stellar motions is a powerful way to measure the properties of tidal streams (e.g., Koposov et al. 2019) and bulk motions within the Galaxy.

In order to develop the capability to measure stellar proper motions, especially at brightnesses up to 5 mag fainter than Gaia (Gaia Collaboration et al. 2016), and better understand the systematics floor that arises, we have undertaken joint processing on prototype data sets in the  $1.64 \text{ deg}^2$  Cosmological Evolution Survey (COSMOS)<sup>3</sup> field (Scoville et al. 2007). In particular, the COSMOS field has data over a decade in time, first from the Hubble Space Telescope (HST) Advanced Camera for Surveys (ACS; Koekemoer et al. 2007)<sup>4</sup> and, more recently, from the Subaru Telescope Hyper Suprime-Cam (HSC; Aihara et al. 2018; Miyazaki et al. 2018)<sup>5</sup> with a spatial resolution of  $\sim 0''.1$  and  $0''.7$ , respectively (Koekemoer et al. 2007; Aihara et al. 2018).

In this paper, we measure and analyze stellar proper motions in the COSMOS field. We do this by first bringing the ACS/F814W and HSC  $i$ -band data, which have an epoch differential of about 11 yr, into astrometric concordance. We use Gaia Data Release 2 (DR2; Gaia Collaboration et al. 2018) sources within COSMOS as a benchmark comparison of our measured proper motions at bright magnitudes. The greater sensitivity of ACS and HSC photometry affords the potential to increase the number of proper-motion sources in the field and extend the volume covered by them.

Our aim for these studies is to understand the spatial distribution and velocities of a large sample of faint stars in the line of sight toward the COSMOS field. The proper motions, coupled with optical colors and information on extinction,

Original content from this work may be used under the terms of the [Creative Commons Attribution 4.0 licence](https://creativecommons.org/licenses/by/4.0/). Any further distribution of this work must maintain attribution to the author(s) and the title of the work, journal citation and DOI.

<sup>3</sup> <https://cosmos.astro.caltech.edu/>

<sup>4</sup> <https://www.stsci.edu/hst/instrumentation/acs>

<sup>5</sup> <https://www.naoj.org/Projects/HSC/>

allow us to estimate distances to and absolute magnitudes of these faint stars using extrapolations from the known parallaxes of brighter Gaia DR2 sources. Therefore, we can study the velocities of many faint stars as a function of spectral type and luminosity class. Grillmair (2017) discovered ancillary Galactic streams within the Orphan stream complex in the Sagittarius South arm using Sloan Digital Sky Survey (SDSS; York et al. 2000) data. In particular, the Sangarius stream within this complex partially crosses the COSMOS field. Grillmair (2017) did not detect sources in Gaia Data Release 1, in the Sangarius stream, because of insufficient sensitivity. One of our goals is to search for members of this stream in both Gaia DR2 and JSP by leveraging the more numerous and fainter sources, which have astrometry measured through the latter. Qiu et al. (2021) analyzed stellar proper motions at distances up to  $\sim 100$  kpc in an area of  $\sim 100$  deg<sup>2</sup>, including part of the Sagittarius stream, by cross-correlating HSC and SDSS astrometry. Qiu et al. (2021) found that within  $\sim 1$  kpc, red stars show proper motions consistent with Galactic rotation. Further out, up to  $\sim 5$  kpc, proper motions decrease with increasing distance. At halo distances of  $\sim 10$ – $40$  kpc, the Sagittarius stream affects proper motions. Beyond  $\sim 40$  kpc, halo blue stars exhibit isotropic velocities. Our goals in this paper are analogous to the above study.

Section 2 describes the JSP prototype data set from ACS, HSC, and Gaia DR2 in COSMOS. Section 3 describes how we spatially matched stellar sources between these data sets. Section 4 presents the astrometrically corrected JSP data using the grids of either Gaia DR2 stars or empirically selected compact galaxies as references and the resulting JSP proper motions of sources matched to Gaia DR2 stars. Section 5 presents the proper motions of all JSP sources, of which Gaia DR2 matches are a subset, in the astrometric grid of Gaia DR2. Section 6 discusses the uncertainties in our derived JSP proper motions. Section 7 presents our derivation of stellar space velocities after correcting proper motions for the motion of the Sun relative to the local standard of rest (LSR). Section 8 discusses our results, and Section 9 contains our conclusions.

## 2. Observational Data from Hubble and Subaru

The COSMOS field covers an area between approximately R.A.  $149^{\circ}12$  and  $151^{\circ}12$  and decl.  $1^{\circ}2$  and  $3^{\circ}2$  (Scoville et al. 2007). The Subaru/HSC First Data Release of this field consists of images in  $133 12' \times 12'$  so-called “patches” (Aihara et al. 2018). We utilized the coadded calexp images and catalogs of HSC, where each calexp coadd was obtained from 104 individual exposures (of 300 s each) typically taken within the same night. Each calexp coadd corresponds to a patch. The epochs of each coadd of HSC are in 2015.

The Hubble/ACS observations were taken from HST Cycles 12 and 13 only and span the epoch ranges 2003 October 15–2004 May 21 and 2004 October 15–2005 May 21. For these, we considered the coadded exposures as described in Koekemoer et al. (2007). Each coadded exposure and its catalog correspond to an ACS patch where its location and dimensions have an identical counterpart in HSC. The region of the COSMOS field covered by HSC and ACS common patches is  $\sim 1.64$  deg<sup>2</sup>.

We measured the equatorial coordinates and magnitudes in the HSC *i*-band calexp coadd and ACS F814W-band coadd with SExtractor (Bertin & Arnouts 1996). Magnitudes in this paper are in the AB system (Oke 1974) unless otherwise noted.

The chosen bandpasses are the most sensitive to point sources in these two instruments. The output coordinates from SExtractor were unweighted center-of-light measurements with both aperture photometry and isophotal photometry available. The SExtractor HSC positions were recentered via two-dimensional Gaussian fits because we found, upon visual examination of HSC point sources, that the PSFs exhibited elliptical shapes that were not always centered at the center of light of the respective source. The ACS point-source images did not exhibit such ellipticity or asymmetry. This visual examination of HSC and ACS sources revealed that saturation ensues at magnitudes of  $\sim 18.5$ . The reduced  $\chi^2$  of the two-dimensional Gaussian fits increases rapidly with increasing source brightness starting at  $\sim 18.5$  mag, thus confirming the onset of saturation.

The SExtractor astrometry and photometry of unsaturated sources in ACS and HSC were used in our subsequent analysis, and astrometric corrections were further applied, as described in Section 4.

## 3. Astrometric Matching between ACS, HSC, and Gaia DR2 in the COSMOS Field

In order to assess the astrometry of HSC and ACS that we obtained with SExtractor, we need to cross-correlate it with an independent “standard of truth.” We regard Gaia as one such standard and describe it here and in Section 4.1, while in Section 4.2, we consider an alternative, relative standard consisting of a sample of empirically selected compact galaxies. The COSMOS field was searched in the Gaia DR2 catalog for single and nonvariable sources (using the Gaia DR2 flag conditions *duplicated\_source* = 0 and *phot\_variable\_flag* = NOT\_AVAILABLE). Only sources with a Gaia parallax  $> 0$  were selected, meaning they had a valid solution for proper motion and parallax. Luri et al. (2018) discussed the biases induced when removing Gaia parallaxes  $< 0$  in Gaia sample selections. The effect is to favor the selection of stellar sources at closer distances, to the detriment of those at larger distances from us. Luri et al. (2018) plotted the histogram of the Gaia DR2 parallaxes of 556,849 quasars from the AllWISE survey and showed that their mean was, as expected for these distant sources, close to zero, namely,  $\sim -10$   $\mu$ as. When removing negative parallaxes, the mean was unrealistically large, namely,  $\sim 0.8$  mas. Our sample of sources is much larger than Gaia stars, as will be discussed in Section 5, but we repeated all of our calculations that involved Gaia stars, for comparison, by including all Gaia DR2 parallaxes, even those  $< 0$ . The effects of using all Gaia DR2 parallaxes on our analysis are presented in Sections 4, 6.2, and 7.

In the 133 HSC calexp coadds, 2434 unique sources were spatially matched to Gaia DR2 stars using a  $0''.2$  radius circle. This search radius was chosen because it resulted in successful matches without source confusion and because the Gaia proper motions of unsaturated sources were  $\ll 200$  mas yr<sup>-1</sup>. Duplicate HSC sources in the areas of overlap of adjacent calexp coadds (e.g., Faisst et al. 2022) were already removed. Among the above 133 HSC coadds, 63 were measured in common with ACS. In these 63 HSC coadds, 1514 sources were matched to Gaia DR2 stars as described above. Similarly, 1135 sources in the 63 ACS coadds were matched to Gaia DR2 stars. In each case, the Gaia star positions were propagated to the epoch of each HSC patch, and to the mean epoch of the various individual

exposures that covered each detected ACS source, using their Gaia-measured proper motions, before the above spatial match. Corrections for parallaxes obtained from the Gaia DR2 catalog were also applied during this process.

In Appendix A, we describe the various samples of stars that we have used in our analysis throughout this paper.

For each HSC–Gaia matched pair with separations in R.A. and decl. of, respectively,  $\Delta R.A.(\text{HSC}, \text{Gaia})$ ,  $\Delta \text{decl.}(\text{HSC}, \text{Gaia})$  (in mas) between the two components, the medians  $\langle \Delta R.A.(\text{HSC}, \text{Gaia}) \rangle_{15}$  and  $\langle \Delta \text{decl.}(\text{HSC}, \text{Gaia}) \rangle_{15}$  of this matched pair and up to 14 neighboring ones within  $4'$  were computed. That is, the subscript 15 indicates that up to 15 offset vectors such as  $\Delta R.A.(\text{HSC}, \text{Gaia})$  went into the computation of the median  $\langle \Delta R.A.(\text{HSC}, \text{Gaia}) \rangle_{15}$ . The HSC source was at the center of the  $4'$  radius circle containing its (HSC, Gaia) matched pair and up to 14 neighboring matched pairs. The number of neighbors and the size of the area searched for them were chosen so as to have a sufficient number of sources to calculate statistics and a small enough area so that the median offsets  $\langle \Delta R.A.(\text{HSC}, \text{Gaia}) \rangle_{15}$  and  $\langle \Delta \text{decl.}(\text{HSC}, \text{Gaia}) \rangle_{15}$  were representative of each particular sky position without cross-contamination from other areas. The smallest spatial scale of variations of median offset vectors is  $\sim 2' - 3'$ , as found by visual inspection in both HSC and ACS coadds. The purpose of obtaining median offsets was to assess the astrometric difference between HSC and Gaia DR2 as a function of sky position and subsequently correct the HSC caexp coadd astrometry for any residuals not accounted for during the generation of these coadds. In order to illustrate the variations in median offsets and their dispersion in the COSMOS field, we superposed all 63 HSC patches (that were common to ACS) after transforming the coordinates within each patch to relative coordinates with respect to the patch center. The resulting “stacked patch” had a much higher signal-to-noise ratio (S/N) in the median offset vectors than individual patches and was divided into  $5 \times 5$  “cells” of  $2.4 \times 2.4 \text{ arcmin}^2$  each. Figure 1(a) shows the median, within a cell in the stacked HSC patch, of the median offset vectors  $\langle \Delta R.A.(\text{HSC}, \text{Gaia}) \rangle_{15}$  and  $\langle \Delta \text{decl.}(\text{HSC}, \text{Gaia}) \rangle_{15}$  between HSC and Gaia DR2. Similarly, Figure 1(b) shows the median, within a cell in the stacked ACS patch, of the median offset vectors  $\langle \Delta R.A.(\text{ACS}, \text{Gaia}) \rangle_{15}$  and  $\langle \Delta \text{decl.}(\text{ACS}, \text{Gaia}) \rangle_{15}$  between ACS and Gaia DR2. Figures 1(a) and (b) show that the median offset vector between HSC and Gaia DR2 has a magnitude of  $\sim 65$  mas and points to approximately the NE direction, while that between ACS and Gaia DR2 has a magnitude of  $\sim 80$  mas and points to approximately the ESE direction. The astrometric offset between each of the HSC and ACS data sets and Gaia DR2 is thus to first order a systematic translation. However, these figures also indicate variations from  $2.4 \times 2.4 \text{ arcmin}^2$  cell to cell. The offset vector of HSC in the upper left corner of Figure 1(a) is significantly steeper relative to the W–E direction than in most of the area of an HSC patch, while Figure 1(b) shows that the ACS offset vector in the lower right corner of an ACS patch is practically horizontal (pointing to the E). These variations are due to residuals in the astrometric grids of HSC and ACS coadds, although they are not distortion corrections per se because HSC and ACS patches are not uniquely associated with detectors. Figures 1(a) and (b) illustrate the corrections that can be applied to the astrometric grids of HSC and ACS to bring them into alignment with the Gaia DR2 astrometric grid.

#### 4. Astrometric Corrections of HSC and ACS and Resulting JSP Proper Motions of Gaia DR2 Sources

In this section, we correct the astrometry of HSC and ACS detected sources to the grids of either Gaia DR2 stars or empirically selected compact galaxies.

##### 4.1. Astrometric Correction to the Gaia DR2 Grid

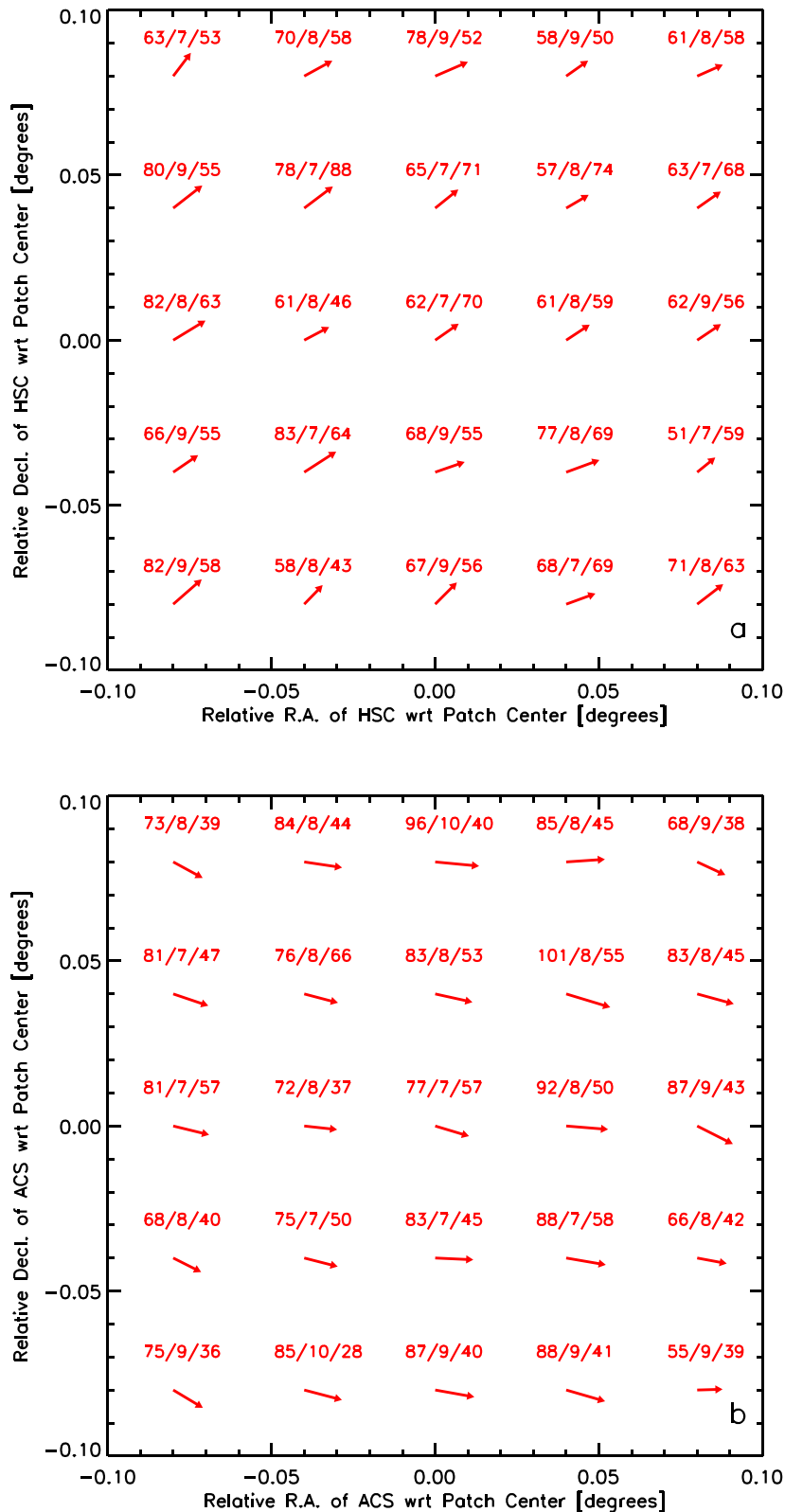
We applied astrometric corrections of ACS and HSC to the Gaia DR2 grid by subtracting, from SExtractor R.A. and decl. coordinates of each source, median offsets  $\langle \Delta R.A.(\text{HSC}, \text{Gaia}) \rangle_{15}$ ,  $\langle \Delta \text{decl.}(\text{HSC}, \text{Gaia}) \rangle_{15}$  (in the case of HSC) and  $\langle \Delta R.A.(\text{ACS}, \text{Gaia}) \rangle_{15}$ ,  $\langle \Delta \text{decl.}(\text{ACS}, \text{Gaia}) \rangle_{15}$  (in the case of ACS), described in Section 3.

Figure 2 shows offsets  $\Delta R.A.(\text{HSC}, \text{Gaia})$  and  $\Delta \text{decl.}(\text{HSC}, \text{Gaia})$  between HSC recentered (Section 2) and astrometrically corrected (to the Gaia DR2 grid) SExtractor sources and Gaia DR2 matched stars, as a function of Gaia  $G$  magnitude (hereafter also referred to as  $G$ ). Owing to the proximity of the epochs of the Gaia and HSC observations, the application of proper motion has a modest but definite effect in reducing the standard deviations of the offsets from  $\sim 15 - 20$  mas in the case of no application of proper motion to  $\sim 5 - 10$  mas after applying proper motion. The offsets have a mean of zero after applying proper motion, as opposed to a mean of up to  $\sim +7$  mas (at the brightest magnitudes) if not applying it. When comparing Figures 1(a) and 2, it can be seen that the application of astrometric correction to the Gaia DR2 grid leads to residual offsets of  $\sim \pm 5$  mas in either R.A. or decl. versus the original offsets of  $\sim +50$  mas in either coordinate axis.

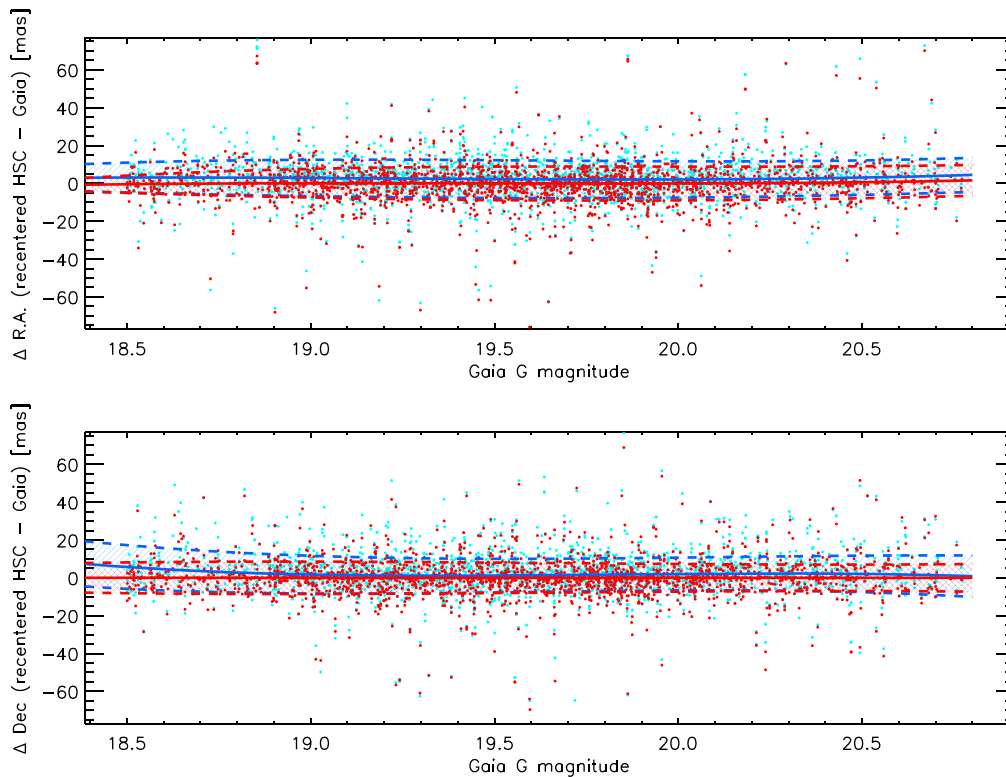
As an illustration of the effect of including all Gaia parallaxes, positive and negative, in the above astrometric corrections of HSC to the Gaia DR2 grid, we found a larger dispersion in the  $\Delta R.A.(\text{HSC}, \text{Gaia})$  and  $\Delta \text{decl.}(\text{HSC}, \text{Gaia})$  offsets at bright  $G$  magnitudes, of  $\sim 10 - 15$  mas, as opposed to only  $\sim 5$  mas when only using positive parallaxes. The dispersion in the offsets was comparable at  $19 < G < 20$  for either positive or all Gaia parallaxes, at  $\sim 5 - 10$  mas. At a  $G$  of 20.7, the dispersion in decl. was larger when using all Gaia parallaxes ( $\sim 10$  mas) than when using only positive ones ( $\sim 5 - 6$  mas).

Figure 3 shows offsets  $\Delta R.A.(\text{ACS}, \text{Gaia})$  and  $\Delta \text{decl.}(\text{ACS}, \text{Gaia})$  between ACS astrometrically corrected (to the Gaia DR2 grid) SExtractor sources and Gaia DR2 matched stars as a function of  $G$ . In this case, owing to the  $\sim 11$  yr difference in the epochs of ACS and Gaia matched stars, the application of proper motion to Gaia stars has a significant effect in reducing the standard deviation of the offsets from  $\sim 100$  mas in the case of no application of proper motion to  $\sim 30$  mas after applying proper motion. The offsets have a mean of zero after applying proper motion, just as in the case of HSC, as opposed to a mean of up to  $\sim +70$  mas if not applying it. When comparing Figures 1(b) and 3, it can be seen that the application of astrometric correction to the Gaia DR2 grid leads to residual offsets of  $\sim \pm 30$  mas in either R.A. or decl. versus the original offsets of  $\sim +70 - 85$  mas in R.A. and 0 to  $\sim -37$  mas in decl.

Both the HSC–Gaia DR2 and ACS–Gaia DR2 residual offsets remain nearly constant with  $G$ . These residual offsets are most likely dominated by systematic effects of the astrometric grid of HSC and ACS, rather than by Poisson statistics of individual sources, as is further discussed in Section 6.



**Figure 1.** (a) The 63 HSC patches common to ACS were superposed or stacked after transforming the equatorial coordinates of all HSC sources to relative coordinates with respect to the center of their respective patch. The red arrows are the median in each  $2.4 \times 2.4$  arcmin<sup>2</sup> cell within an HSC patch of median offset vectors  $\langle \Delta R.A. (HSC, Gaia) \rangle_{15}$  and  $\langle \Delta decl. (HSC, Gaia) \rangle_{15}$  between HSC and Gaia DR2 matched pairs. The  $\langle \Delta R.A. (HSC, Gaia) \rangle_{15}$  and  $\langle \Delta decl. (HSC, Gaia) \rangle_{15}$  were each computed from up to 15 matched pairs within  $4'$  of the source, including the pair of the source itself and its Gaia DR2 match, as described in the text. Sets of three numbers above each vector list its magnitude (mas), one standard deviation of the mean (mas), and the number of median offset vectors in the cell. (b) Similar to panel (a), the 63 ACS patches were superposed, and the red arrows are the median offset vectors in each cell within a patch of median offset vectors  $\langle \Delta R.A. (ACS, Gaia) \rangle_{15}$  and  $\langle \Delta decl. (ACS, Gaia) \rangle_{15}$  between ACS and Gaia DR2 matched pairs. The sets of three numbers above each vector are also as described in panel (a).



**Figure 2.** Offsets in R.A., denoted as  $\Delta R.A.$  (HSC, Gaia) (top panel), or in decl., denoted as  $\Delta \text{decl.}$  (HSC, Gaia) (bottom panel), between HSC SExtractor (recentered via two-dimensional Gaussian fits) and Gaia DR2 catalog coordinates as a function of  $G$  for 2434 sources. Astrometric corrections to the Gaia DR2 grid have been applied as explained in the text. The small red symbols are the offsets (in the sense of HSC–Gaia) after propagating the positions of Gaia DR2 stars to the epochs of HSC coadds and applying Gaia DR2 catalog parallax corrections. The solid red line is the magnitude-binned  $3\sigma$ -clipped mean of the offsets (using a 1 mag boxcar) smoothed with a fourth-order polynomial. The red dashed lines are the upper and lower one standard deviations of these offsets, also magnitude binned and smoothed as above, and the red hatched region represents the  $\pm 1$  standard deviation of these offsets. The small blue symbols, lines, and hatched region are similar offsets and their statistics but without applying proper motion or parallax to Gaia stars.

In turn, the HSC–Gaia matched sources and the ACS–Gaia matched sources were cross-correlated to identify 1010 HSC–ACS matched sources (that is, HSC and ACS sources matched to a common Gaia DR2 star) of  $G$  between 18.5 (that is, unsaturated; see Section 2) and 20.76. The proper motions of these sources were estimated using the SExtractor coordinates of HSC (recentered via two-dimensional Gaussian fits) and ACS, both astrometrically corrected to the Gaia DR2 grid. The epoch of each HSC source was as listed in the FITS header of its calexp coadd. The epoch of each ACS source is the mean of the epochs of single exposures of Cycles 12 and 13 that covered this source. The resulting proper motions are referred to as JSP or HSC–ACS in what follows, to distinguish them from Gaia DR2. The JSP proper motions are not affected by the effect of differential chromatic refraction (Filippenko 1982). The HSC is equipped with an atmospheric dispersion corrector, which partially corrects for the effect, while ACS space-based data are not affected by the Earth’s atmosphere.

We compared the JSP proper motions of the 1010 HSC–ACS–Gaia DR2 matches fainter than  $G = 18.5$  with their Gaia DR2 catalog proper motions. Figures 4(a) and (b) show the correlation between R.A. and decl. proper motions in JSP against Gaia DR2. A dashed line shows a one-to-one correlation, and a solid line shows a least-squares linear fit. It can be seen that JSP and Gaia DR2 proper motions are reasonably correlated; the fit has a slope within  $\sim 3\%$  of a one-to-one correlation with an uncertainty of  $\sim 1\%$ , and the  $y$ -intercept is  $\sim 0.16\text{--}0.18 \text{ mas yr}^{-1}$ . In Section 6, we analyze what these statistics suggest for R.A. and decl. JSP proper

motions. We also explain in Section 6 why the majority but not all of the 1010 sources were plotted in Figure 4.

The use of all Gaia parallaxes, regardless of whether they were positive or negative, yielded the same conclusions on the correlation of JSP and Gaia proper motions as above when using only positive parallaxes.

#### 4.2. Astrometric Correction from Empirically Selected Compact Galaxies

An alternative for astrometrically correcting JSP data is to use extragalactic point sources. Quasars, which would be optimal because they are stationary point sources, are very sparse, with only  $\sim$ one to three expected in the COSMOS field. There are 297 unobscured broad-line active galactic nucleus (BLAGN) compact sources in the catalog of optical/IR counterparts (Marchesi et al. 2016) to the 4016 sources in the COSMOS-Chandra Legacy Survey (Civano et al. 2016). Thus, there are significantly fewer sources than Gaia stars. We generated a much larger sample by empirically selecting compact galaxies in the ACS coadds, where the source image ratio of semiminor to semimajor axes is  $>0.9$ , the SExtractor half-light radius is in the range of 3–5 pixels (to exclude stars whose images are significantly smaller), the SExtractor photometric S/N in the F814W filter is  $>25$ , and the SExtractor magnitude in this bandpass is  $>20$  (again to exclude bright stars and avoid saturation). Faisst et al. (2022) described the resulting ACS sample of 4844 empirically selected compact galaxies.

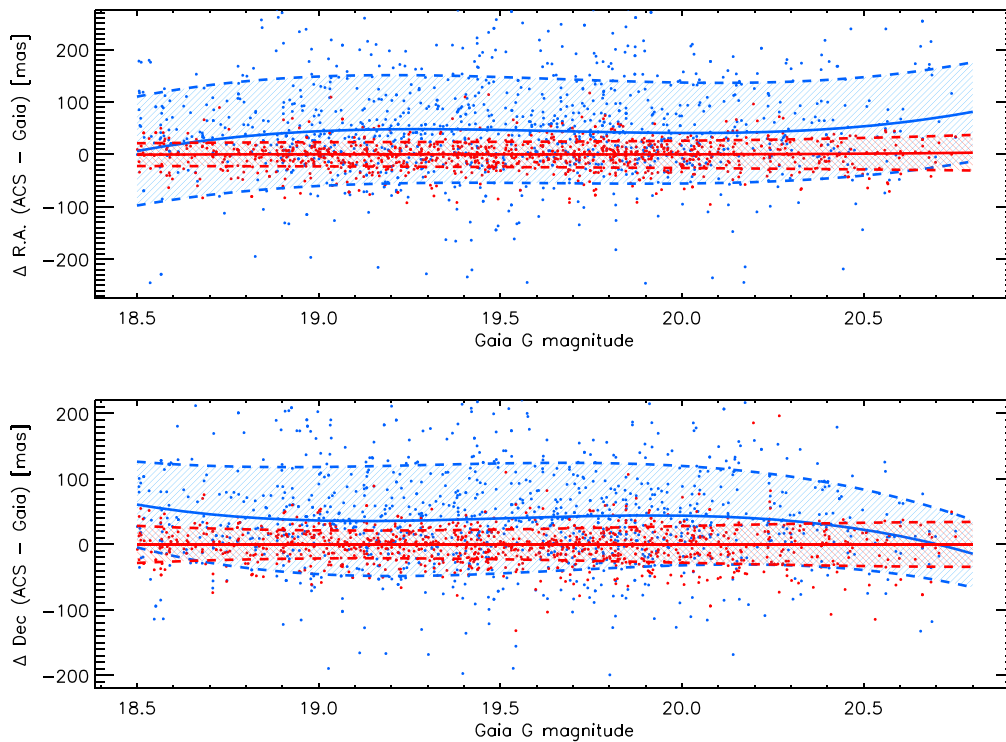


**Figure 3.** Offsets in R.A., denoted as  $\Delta R.A.$  (ACS, Gaia) (top panel), or decl., denoted as  $\Delta \text{decl.}$  (ACS, Gaia) (bottom panel), between ACS SExtractor and Gaia DR2 catalog coordinates as a function of  $G$  for 1135 sources. The small red symbols are the offsets (in the sense of ACS–Gaia) after propagating the positions of Gaia DR2 stars to the mean epoch of all ACS single exposures that covered a given matched ACS source. The solid red line is the magnitude-binned  $3\sigma$ -clipped mean of the offsets after applying proper motion (using a 1 mag boxcar), smoothed with a fourth-order polynomial. The red dashed lines are the upper and lower one standard deviations of these offsets, also magnitude binned and smoothed as above, and the red hatched region represents the  $\pm 1$  standard deviation of these offsets. The small blue symbols, lines, and hatched region are similar offsets and their statistics but without propagating the positions of Gaia stars.

This sample was spatially matched to SExtractor HSC sources, using a  $0''.2$  radius circle, to find 4236 matches fainter than AB mag 18.5. As we do not expect a measurable mean motion for these extragalactic objects, the offsets between HSC and ACS should ideally be zero. In reality, owing to residuals not accounted for in the generation of the coadds, nonzero offsets were found.

We denote by  $\Delta R.A.$  (HSC, ACS) and  $\Delta \text{decl.}$  (HSC, ACS) the separations in R.A. and decl. (in mas), respectively, between the two components of an HSC–ACS compact galaxy matched pair. For each matched pair, we then compute the median of  $\Delta R.A.$  (HSC, ACS) and those of up to 14 neighboring matched pairs within  $4'$  and denote it by  $\langle \Delta R.A. (\text{HSC}, \text{ACS}) \rangle_{15}$  (and a similar median in decl. denoted by  $\langle \Delta \text{decl.} (\text{HSC}, \text{ACS}) \rangle_{15}$ ). The purpose of obtaining these median offset vectors  $\langle \Delta R.A. (\text{HSC}, \text{ACS}) \rangle_{15}$  and  $\langle \Delta \text{decl.} (\text{HSC}, \text{ACS}) \rangle_{15}$  was, in analogy to Section 3, to assess the astrometric difference between HSC and ACS as a function of sky position and, in particular, variations across the region covered by a  $12 \times 12$  arcmin<sup>2</sup> patch. These median offsets allow us to correct the HSC calexp coadd astrometry for any residuals not accounted for during the generation of the calexp coadds. That is, just as in Section 3, where Gaia DR2 stars were considered the standard of truth, in this case, ACS compact galaxies were considered a relative standard (of HSC with respect to ACS). We superposed all 63 HSC patches common to ACS (Section 2) and divided the resulting stacked patch into  $5 \times 5$  cells. Figure 5 shows the median within each cell of the median offset vectors  $\langle \Delta R.A. (\text{HSC}, \text{ACS}) \rangle_{15}$  and  $\langle \Delta \text{decl.} (\text{HSC}, \text{ACS}) \rangle_{15}$  for HSC–ACS compact galaxy matches (blue arrows). For comparison, Figure 5 also shows,

as red arrows, the median within each cell of the difference (separately in R.A. and decl.) between median offset vectors  $\langle \Delta R.A. (\text{HSC}, \text{Gaia}) \rangle_{15}$ ,  $\langle \Delta \text{decl.} (\text{HSC}, \text{Gaia}) \rangle_{15}$  and median offset vectors  $\langle \Delta R.A. (\text{ACS}, \text{Gaia}) \rangle_{15}$ ,  $\langle \Delta \text{decl.} (\text{ACS}, \text{Gaia}) \rangle_{15}$ . Figures 1(a) and (b) separately showed the medians within each cell of the two quantities that were subtracted above. Ideally, if the astrometric corrections of HSC and ACS to the Gaia DR2 grid and the astrometric correction of HSC to the ACS compact galaxies grid were equivalent, then the relation  $\Delta R.A. (\text{HSC}, \text{Gaia}) - \Delta R.A. (\text{ACS}, \text{Gaia}) = \Delta R.A. (\text{HSC}, \text{ACS})$  (and separately in decl. also) would be exact, and the blue and red arrows in Figure 5 would be identical.

Figure 5 shows that the blue and red arrows agree to within 10% in magnitude but with excursions as high as 70% and within  $15^\circ$  in position angle but with excursions as high as  $50^\circ$ . Therefore, the astrometric corrections to the Gaia DR2 grid and the grid of ACS compact galaxies are in reasonable agreement, but the above differences are used in Section 6 to quantify the contribution of the astrometric grid correction uncertainty to that of JSP proper motions.

The median offset vector between HSC and ACS compact galaxies has a magnitude of  $\sim 50$  mas and points to approximately the NNW direction and is therefore, to first order, a systematic translation. However, there are variations across the region of patches. Four of the cells exhibit median per-source offset vectors pointing to the NNE direction. These variations are due to residuals in the astrometric grid of HSC relative to ACS, and Figure 5 suggests corrections that can be applied to the HSC astrometric grid to bring it into relative alignment with the ACS astrometric grid. In this approach, the ACS grid would remain uncorrected.

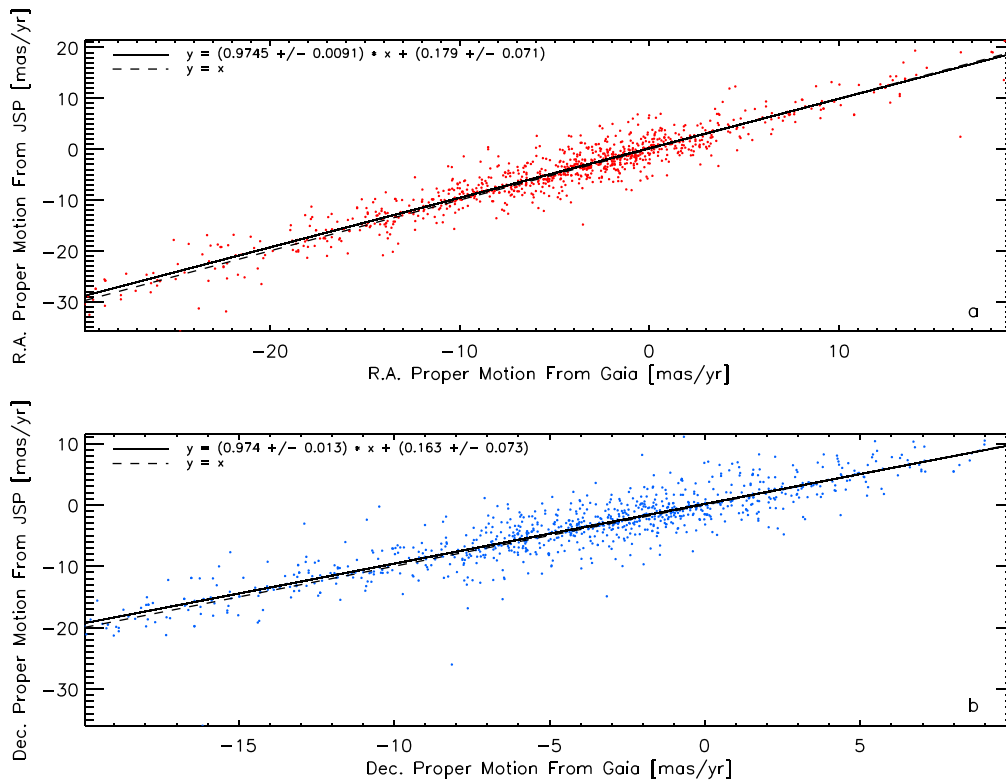


**Figure 4.** Correlation of proper motions from JSP (estimated from HSC and ACS in this work) and the Gaia DR2 catalog for sources fainter than 18.5 Gaia DR2 magnitude. The red symbols are proper motions in R.A., and the blue symbols are proper motions in decl. The HSC and ACS astrometry was corrected to the grid of Gaia DR2 stars whose positions were propagated to the epochs of HSC and ACS, as explained in the text. The solid lines are least-squares linear fits, with parameters (slope, y-intercept, and standard deviations) listed in the figure. The dashed lines have unity slopes and represent perfect correlations. Panel (a) shows the correlation of R.A. proper motion from JSP as a function of R.A. proper motion from Gaia DR2 for 972 sources with Gaia R.A. proper motion in the range  $-30$  to  $+20$   $\text{mas yr}^{-1}$ . Panel (b) shows the correlation of decl. proper motion from JSP as a function of decl. proper motion from Gaia DR2 for 925 sources with Gaia decl. proper motion in the range  $-20$  to  $+10$   $\text{mas yr}^{-1}$ .

We applied the astrometric correction of the HSC grid to the ACS grid of compact galaxies suggested by Figure 5 by subtracting the median offsets  $\langle \Delta \text{R.A. (HSC, ACS)} \rangle_{15}$  and  $\langle \Delta \text{decl. (HSC, ACS)} \rangle_{15}$  from the SExtractor coordinates of each HSC source. The JSP proper motions of 1010 Gaia DR2 stars were obtained as in Section 4.1. We then cross-correlated these JSP proper motions to the Gaia DR2 catalog proper motions. Figures 6(a) and (b) show these correlations in R.A. and decl., respectively. We can see that the correlations are very comparable to those using astrometry corrected to the grid of Gaia DR2 stars (Figures 4(a) and (b)). In particular, the slopes of the correlations to the Gaia DR2 catalog proper motions are within 1% of each other in the two astrometric grids. The errors of the slope and y-intercepts agree to within 10%. The y-intercepts are within  $\pm 0.3$   $\text{mas yr}^{-1}$ , although smaller in absolute value for the Gaia DR2 astrometric grid ( $\sim 0.16$ – $0.18$   $\text{mas yr}^{-1}$ ) than the ACS compact galaxies grid ( $\sim -0.31$  to  $+0.14$   $\text{mas yr}^{-1}$ ).

### 5. Proper Motions of All JSP Sources, Astrometrically Corrected to the Gaia DR2 Grid

The astrometric potential of JSP is realized by measuring the proper motions of a vast number of stellar sources fainter than Gaia. To predict the number of expected sources, we ran the Wainscoat et al. (1998) star count model for the COSMOS field (Figure 7, black line). This model has been scaled to the common area covered by HSC and ACS (Section 2). We find that the total number of stars expected from the model brighter

than 25 AB mag is  $1.7 \times 10^4$  and that between 19 and 25 AB mag is  $1.3 \times 10^4$ .

In order to build a large sample of stars in the COSMOS field, we first identified 13,009 sources in the ACS coadds that were empirically determined to be stars (Figure 7, red line). These sources have SExtractor magnitudes in the F814W filter between 19 and 26, they have a “round” morphology (i.e., the ratio of semiminor to semimajor axes is  $> 0.9$ ), their SExtractor flag CLASS\_STAR is  $> 0.9$ , and they satisfy SExtractor  $S/N > 30$ . In addition, these sources were required to be located in a plot of SExtractor half-light radius of the source image in the ACS coadds as a function of SExtractor magnitude (Figure 8), below the 84th percentile of the distribution that was fit in the range 19–22.5 AB.

To the sample of ACS empirically selected stars, we added 3937 ACS stars matched to Gaia DR2 stars, unconstrained in apparent magnitude or parallax. From this sample, we then removed 453 sources that were already included in the empirically selected stars. Otherwise, the remaining ACS stars matched to Gaia DR2 stars were not among the ACS empirically selected stars mainly because they are brighter than 19 AB magnitude. Thus, our starting large sample of ACS stars consists of 16,493 sources (Figure 7, red line). The number of these stars brighter than 25 AB mag is  $1.6 \times 10^4$  and that between 19 and 25 AB mag is  $1.3 \times 10^4$ . These numbers are in very good agreement (10% or better) with the above predictions from the Wainscoat model. The histogram of our large sample of ACS stars is shown as a red line in Figure 7, where the agreement with the Wainscoat model is 10% or

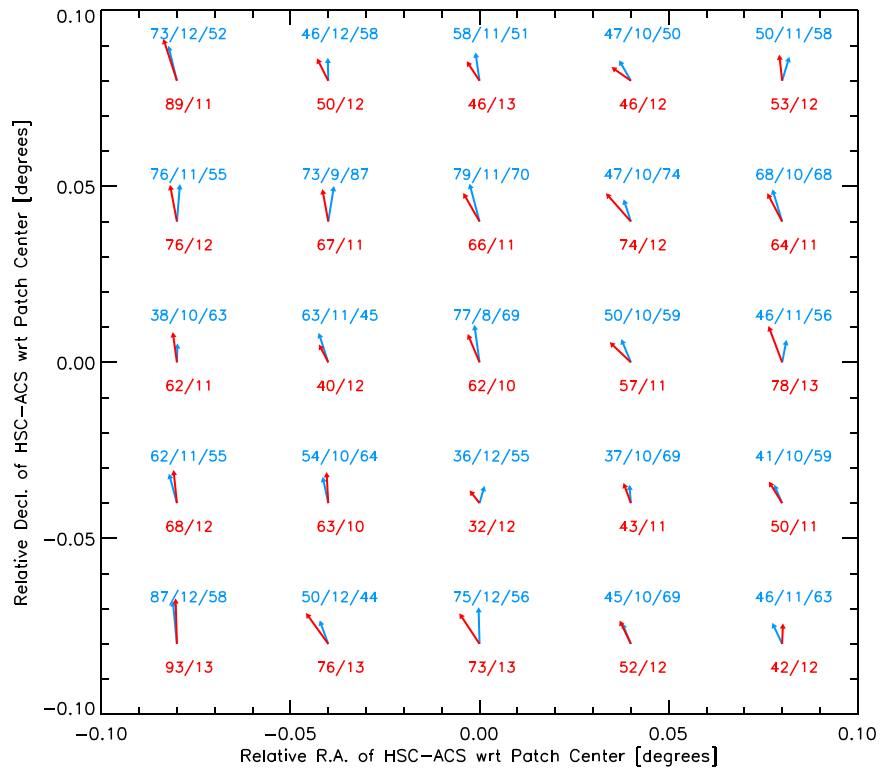


**Figure 5.** The 63 HSC patches common to ACS were superposed or stacked after transforming the equatorial coordinates of all HSC sources to relative coordinates with respect to the center of their respective patch (see Section 3). The blue arrows are the median in each  $2.4 \times 2.4$  arcmin<sup>2</sup> cell within the stacked HSC patch of median offset vectors  $\langle \Delta R.A. (HSC, ACS) \rangle_{15}$  and  $\langle \Delta \text{decl.} (HSC, ACS) \rangle_{15}$  between HSC and ACS compact galaxy matched pairs. The median offset vectors were computed from up to 15 matched pairs within  $4'$  of the source, including the pair of the HSC source itself and its ACS match, as described in the text. Sets of three numbers (in blue) above each vector list its magnitude (mas), one standard deviation of the mean (mas), and the number of median offset vectors in the cell. For comparison, the red arrows are the median of the difference (separately in R.A. and decl.) within each cell between median offset vectors  $\langle \Delta R.A. (HSC, Gaia) \rangle_{15}$ ,  $\langle \Delta \text{decl.} (HSC, Gaia) \rangle_{15}$  and median offset vectors  $\langle \Delta R.A. (ACS, Gaia) \rangle_{15}$ ,  $\langle \Delta \text{decl.} (ACS, Gaia) \rangle_{15}$ . The sets of two numbers (in red) above each vector list its magnitude (mas) and one standard deviation of the mean (mas).

better up to AB mag 25. Stars fainter than 25 in our sample precipitously drop in numbers because of our S/N SExtractor threshold.

In the HSC SExtractor catalog, we spatially matched 11,783 sources to the 13,009 ACS empirically selected faint stars using a  $0''.2$  radius circle. The HSC and ACS positions were previously astrometrically corrected to the Gaia DR2 reference, as explained for Gaia matches in Section 4.1. We then computed their JSP proper motions and added them to the sample of 1010 JSP proper motions of Gaia stars with positive parallaxes (Section 4.1). Excluding 264 JSP proper motions of Gaia stars common to the above samples, we finally have a sample of 12,529 sources fainter than AB 18.5 mag with well-determined JSP proper motions.

Of the 1010 Gaia–ACS stars with well-determined proper motions in the above sample, 746 were not detected in our empirical selection of faint stars. The reason is that  $\sim 80\%$  of the 1010 Gaia–ACS sources had an SExtractor AB mag brighter than 19 and were thus excluded by definition from the empirically selected faint stars. Of the remaining  $\sim 20\%$ , half of them had anomalously high noise values, and the remaining half did not satisfy the “roundness” criterion described above.

In Sections 6 and 7, we analyze the uncertainties of our derived JSP proper motions for the above large sample of stars and our derivation of velocities and distances to these stars, respectively.

An alternative to the astrometric correction to the Gaia DR2 grid is to correct to the grid of 4844 empirically selected compact galaxies, as described in Faisst et al. (2022); see

Section 4.2. Section 4.2 shows that this correction, when applied to Gaia stars, yields comparable results to a correction to the Gaia DR2 grid. We also applied such a correction to our set of 11,519 empirically selected faint stars and derived JSP proper motions very similar to those when corrected to the grid of Gaia DR2.

Owing to the similarity of JSP proper motions using either the grid of Gaia DR2 stars or that of compact galaxies, we confine our remaining analysis to the former. However, we still utilize the latter (correction to the grid of ACS compact galaxies) to estimate the systematic uncertainties of the astrometric grid correction, as explained in Section 6.

## 6. Uncertainties in JSP Proper Motions

In this section, we analyze the uncertainties in JSP proper motions using several approaches: (i) taking the comparison of JSP and Gaia DR2 proper motions described in Section 4.1, (ii) combining Monte Carlo simulations of centroiding uncertainties and differences in astrometric corrections to the grids of Gaia DR2 and empirically selected compact galaxies (Sections 4.1 and 4.2), and (iii) computing the residuals of JSP “null motions” of stationary extragalactic sources.

### 6.1. Monte Carlo Simulations of JSP versus Gaia Proper Motions

In Section 4.1, we compare JSP and Gaia DR2 catalog proper motions, and the results are shown in Figure 4. We carried out Monte Carlo simulations of Figures 4(a) and (b)

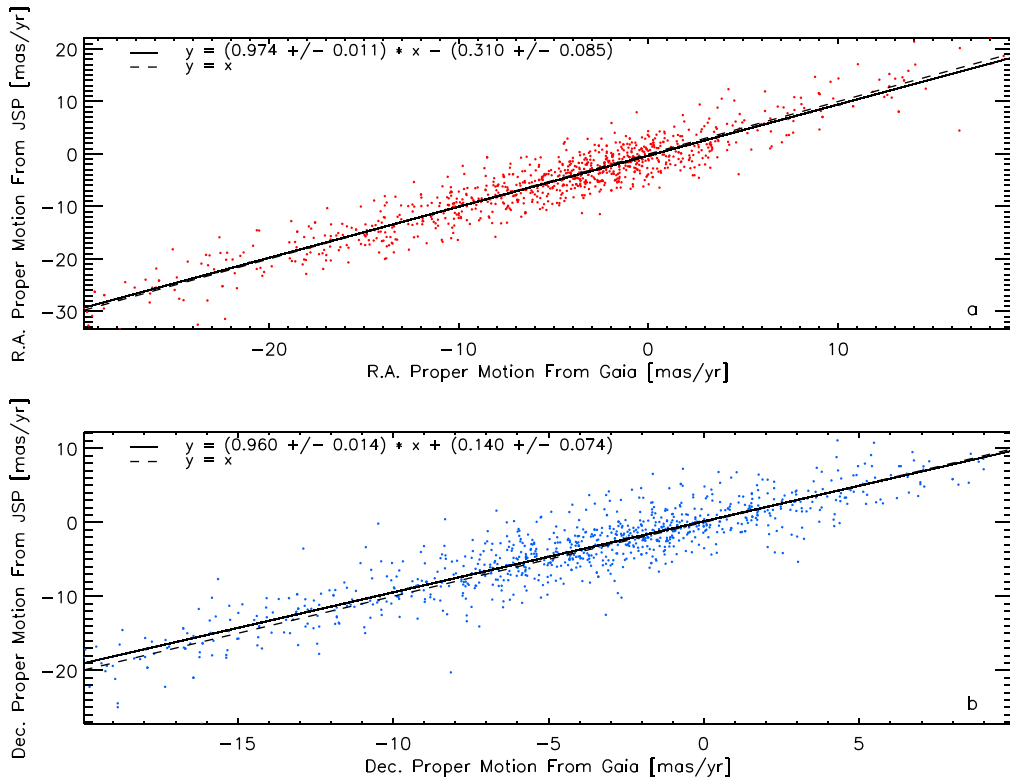


**Figure 6.** Correlation of proper motions from JSP (estimated from HSC and ACS in this work) and the Gaia DR2 catalog for sources fainter than 18.5 Gaia DR2 magnitude. The red symbols are proper motions in R.A., and the blue symbols are proper motions in decl. The HSC astrometry was corrected to the grid of ACS compact galaxies described in the text and Faisst et al. (2022). The solid lines are least-squares linear fits with parameters (slope, y-intercept, and standard deviations) listed in the figure. The dashed lines have unity slopes and represent perfect correlations. Panel (a) shows the correlation of R.A. proper motion from JSP as a function of R.A. proper motion from Gaia DR2 for 971 sources with Gaia R.A. proper motion in the range  $-30$  to  $+20$   $\text{mas yr}^{-1}$ . Panel (b) shows the correlation of decl. proper motion from JSP as a function of decl. proper motion from Gaia DR2 for 925 sources with Gaia decl. proper motion in the range  $-20$  to  $+10$   $\text{mas yr}^{-1}$ .

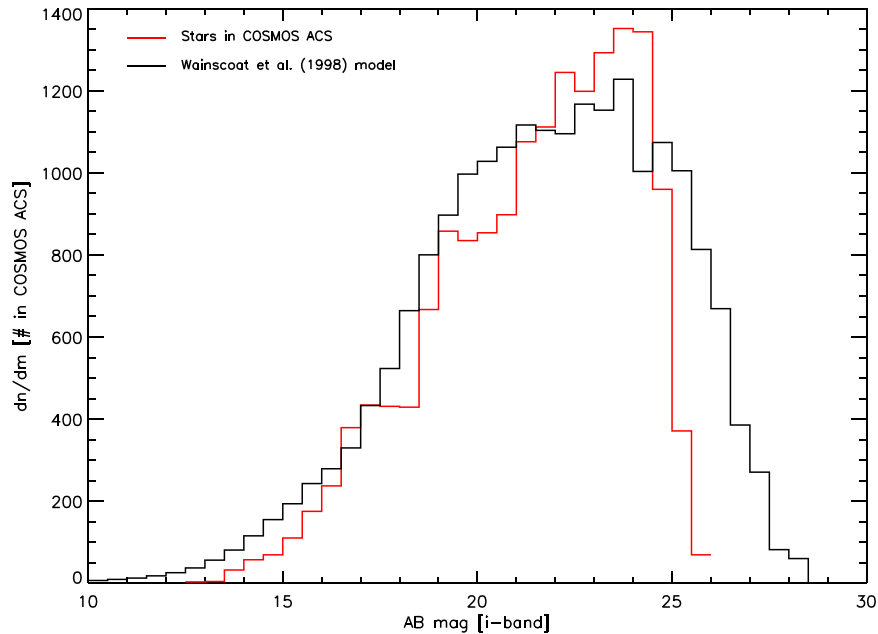


**Figure 7.** The black line is the histogram of expected stellar source count as a function of AB mag in the COSMOS field, computed from the model by Wainscoat et al. (1998). The red line is the number of empirically determined stars in this field detected by ACS, as described in the text, and a separate sample detected by ACS and matched to Gaia DR2.

separately by generating 50 Gaussian-distributed random proper-motion deviants relative to a perfect correlation of JSP and Gaia DR2 proper motions. Our free parameter was the standard deviation of JSP proper-motion distributions. The

standard deviations of Gaia proper motions were those from the Gaia DR2 catalog. For each JSP standard deviation, least-squares linear fits were estimated to the resulting Monte Carlo simulated JSP versus Gaia proper-motion correlation. Our goal

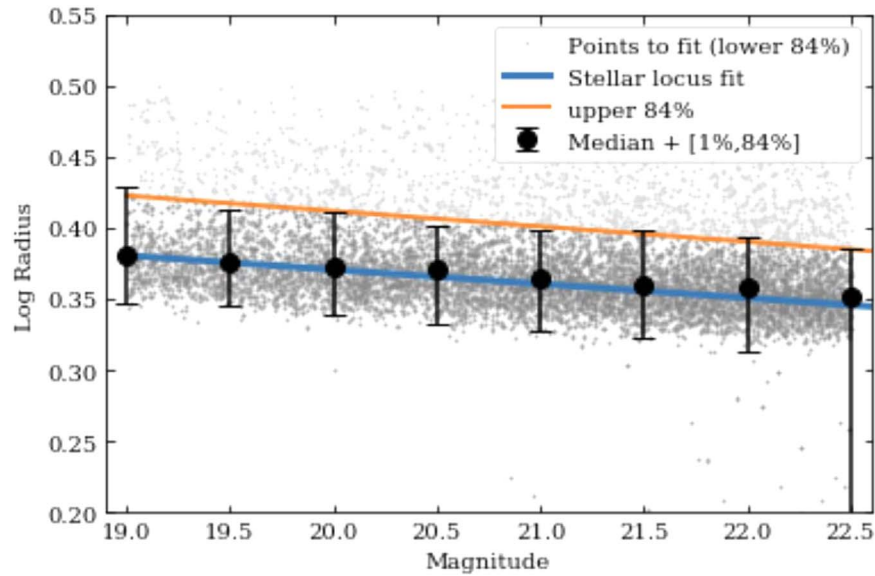


**Figure 8.** The plot shows the technique used for empirical selection of faint stars. The y-axis shows the SExtractor half-light source radius (in pixels). A linear fit (blue line) was obtained to the magnitude-binned median half-light source radius (in pixels) as a function of SExtractor F814W ACS AB magnitude. The error bars are the magnitude-binned 1st and 84th percentiles of the distribution. The orange line is a linear fit to the 84th percentiles, and sources below it are considered to be stars.

was to match the simulation linear fit parameters to those in Figures 4(a) and (b). Among the various simulations we tried, standard deviations in R.A. and decl. JSP proper motion of  $2.0 \text{ mas yr}^{-1}$  each yield the closest match to the actual proper-motion linear fits. These uncertainties are per axis (either R.A. or decl.) and apply to all sources; therefore, they are an approximation.

### 6.2. Combination of Centroiding and Astrometric Grid Correction Uncertainties

An estimate of the uncertainty in the proper motion by combining the uncertainty of centroiding and that from systematics in the correction to the grid of Gaia DR2 may be more accurate than that from the linear correlation of JSP and Gaia described above.

The centroiding uncertainty of HSC was estimated by running Monte Carlo simulations on one patch, namely, (5, 4) (see Aihara et al. 2018 for an explanation of patch nomenclature). Detected objects from SExtractor were masked, and 10,000 random positions were generated, falling outside the masked positions. The PSFs in the magnitude range 19–26.5 were generated and placed at the above random positions, and SExtractor was run on these artificial sources. The difference between the input random position and the SExtractor position for each artificial source was computed. The magnitude-binned standard deviations of these differences are shown as error bars in Figure 9. We regard these uncertainties as representing the centroiding uncertainty of HSC. The corresponding centroiding uncertainty of ACS is  $\sim$ one-sixth that of HSC because this is the ratio of pixel sizes in HSC and ACS ( $0''.168$  and  $0''.030$ , respectively).

The contribution of centroiding uncertainty to JSP proper-motion uncertainty is estimated from Figure 9. Since there are  $\sim 11$  yr separating the epochs of ACS and HSC, for a given HSC centroiding uncertainty  $\sigma_{\text{HSC,centr}}$ , as in the error bars in Figure 9, the corresponding uncertainty in JSP proper motion,

which includes the ACS centroiding uncertainty, is

$$\sigma_{\text{JSP,centr}} = \frac{\sigma_{\text{HSC,centr}}}{11} \sqrt{1 + \left(\frac{1}{6}\right)^2} = \frac{\sqrt{37}}{66} \sigma_{\text{HSC,centr}}. \quad (1)$$

These uncertainties in proper motion arising from centroiding are shown in Figure 10 as symbols connected with dotted lines. They generally increase with increasing magnitude, from  $\sim 0.9$  to  $\sim 6.2 \text{ mas yr}^{-1}$  in total JSP proper motion.

We estimated the uncertainty of the JSP proper motions arising out of systematics in astrometric grid correction by finding the JSP proper-motion difference for each source after correcting to both the Gaia DR2 grid (Sections 4.1 and 5) and the grid of empirical compact galaxies (Section 4.2). These differences were binned by SExtractor ACS magnitude (in the F814W bandpass), and their standard deviations as a function of magnitude are shown in Figure 10 as symbols connected by dashed lines. These standard deviations represent the portion of uncertainty of JSP proper motions arising out of the uncertainty of astrometric correction of HSC and ACS (i.e., when comparing the astrometric corrections with respect to both Gaia DR2, Section 5, and empirical compact galaxies, Section 4.2). Possible sources of these systematic uncertainties are uncertainties in the Gaia DR2 proper motions and contamination of the sample of compact galaxies with some stellar objects. The systematic uncertainties in astrometric grid correction are  $\sim 2.0$ – $3.05 \text{ mas yr}^{-1}$  in R.A. and nearly constant with magnitude or  $\sim 1.9$ – $2.1 \text{ mas yr}^{-1}$  in decl. The larger variation in R.A. proper-motion uncertainty, increasing toward brighter sources, is due to the systematic uncertainty in two-dimensional Gaussian fitting of sources close to saturation and the fact that the absolute value of the astrometric corrections in R.A. relative to Gaia DR2 are larger than in decl. (Figures 1(a) and (b)). The total contribution to the JSP proper-motion uncertainty (quadrature combination of R.A. and decl. components) from astrometric grid correction is in the range of  $\sim 3.0$ – $3.9 \text{ mas yr}^{-1}$ .

We believe that the total uncertainties in JSP proper motions, from both centroiding and astrometric grid corrections and

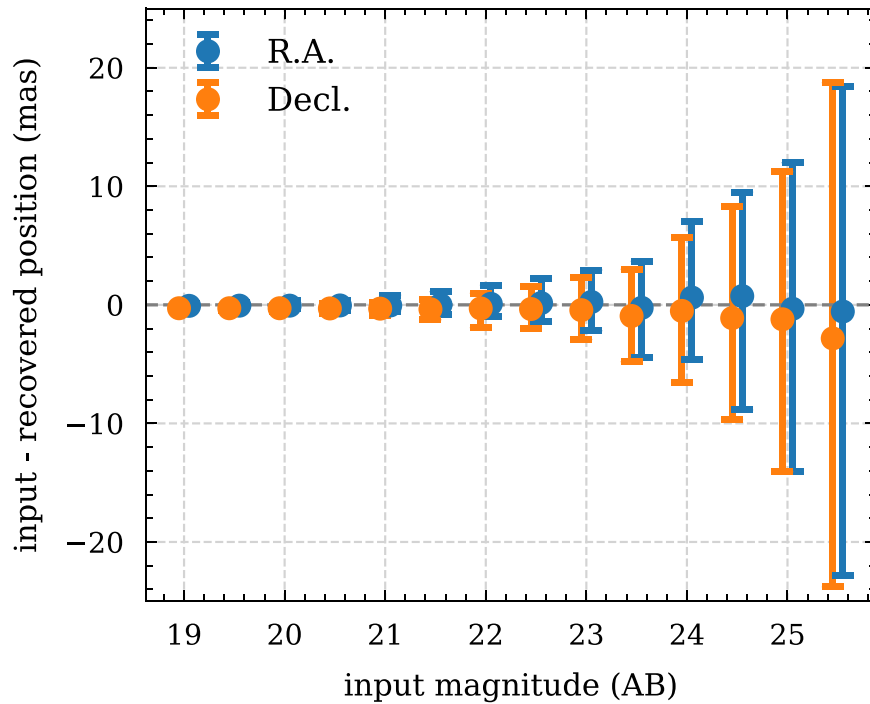


**Figure 9.** Monte Carlo simulation of centroiding uncertainty in HSC. Plotted are the magnitude-binned positional differences between randomly generated point sources and their SExtractor recovered positions, separately in R.A. (blue symbols) and decl. (orange symbols), as a function of SExtractor HSC  $i$  magnitude. The error bars are one standard deviations of these differences in each magnitude bin.

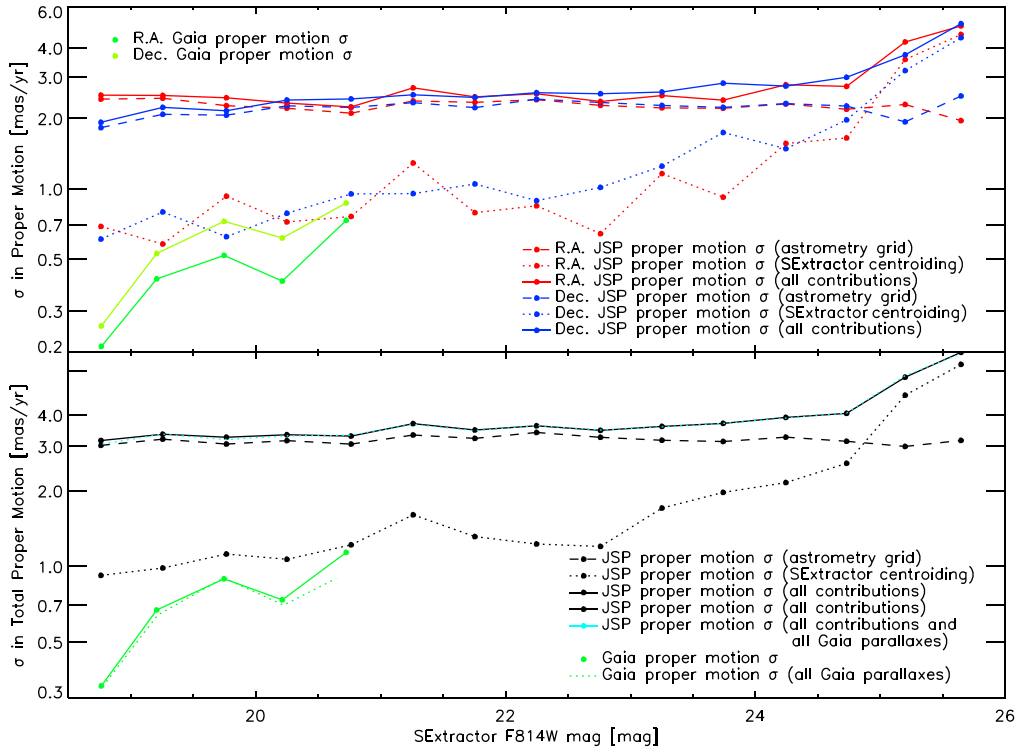


**Figure 10.** Uncertainties in JSP proper motions. The top panel shows uncertainties in each axis (red symbols connected with red lines are for R.A., and blue symbols connected with blue lines are for decl.). For comparison, the Gaia DR2 catalog proper-motion uncertainties are shown as aquamarine symbols connected with aquamarine lines for R.A. and green symbols connected with green lines for decl. These uncertainties were computed in 0.5 mag wide bins, where the photometry is from SExtractor in the ACS F814W bandpass. The JSP uncertainties from centroiding are shown as symbols connected with dotted lines, and the uncertainties from astrometric grid correction of HSC and ACS patches, as explained in the text, are shown as symbols connected with dashed lines. The JSP uncertainties from both of these contributions are shown as symbols connected with solid lines. The bottom panel shows uncertainties in total (R.A. and decl. combined in quadrature), JSP (black symbols), and Gaia DR2 catalog (green symbols) proper motions. The bottom panel also shows, for comparison, uncertainties in the total JSP (light blue symbols connected with a dotted line) and Gaia DR2 catalog (green dotted line) proper motions when using all Gaia stars, regardless of whether their parallaxes were positive or negative.

applying to the quadrature combination of R.A. and decl. proper motions, are as shown by symbols connected with solid lines in the bottom panel of Figure 10. They generally increase with increasing magnitude and range from  $\sim 3$  to  $\sim 4$  mas yr $^{-1}$  in the magnitude range 18.5–25. The portion of uncertainty from centroiding starts to dominate over astrometric grid correction at  $\sim 25$  mag, and the total uncertainty is as high as  $\sim 6.5$  mas yr $^{-1}$  at 26 mag. We therefore confined our analysis to stars as faint as 25 mag.

The bottom panel of Figure 10 also shows, for comparison, the total uncertainties in JSP proper motions, shown as light blue symbols connected with a light blue dotted line, when including all Gaia DR2 stars, irrespective of whether their parallaxes were positive or negative. The total uncertainties are almost indistinguishable when including all Gaia parallaxes during the astrometric grid correction relative to when including only positive parallaxes. The bottom panel of Figure 10 also shows the Gaia DR2 catalog proper-motion uncertainties (green dotted line) for all Gaia parallaxes, including negative ones. These uncertainties are smaller than when including only positive Gaia parallaxes, particularly for the faintest Gaia stars.

### 6.3. Measuring Null Motions of Extragalactic Point Sources

A third method to estimate the uncertainties of JSP proper motions is to astrometrically correct the HSC and ACS positions of unobscured BLAGNs and compute “pseudo-proper motions” by subtracting the HSC and ACS positions and dividing by their epoch difference, just as we did for stellar sources. The sample of 296 BLAGNs (Civano et al. 2016; Marchesi et al. 2016) is as described in the beginning of Section 4.2. Figure 11(a) shows a histogram of the JSP pseudo-proper motions of BLAGNs. The R.A. pseudo-proper motion distribution peaks at 0 mas yr $^{-1}$ , while the decl. one peaks at  $\sim 1$ –2 mas yr $^{-1}$ . Both distributions have FWHM  $\sim 3$ –4 mas yr $^{-1}$ , comparable to our other estimates of uncertainties.

For comparison, Figure 11(b) shows a histogram of the JSP proper motions of 12,529 stars (both Gaia DR2 sources, Section 4.1, and empirically selected faint stars, Section 5). The R.A. proper-motion distribution peaks at  $\sim -1$  mas yr $^{-1}$  with a FWHM of  $\sim 10$  mas yr $^{-1}$ , while the decl. one peaks at  $\sim -4$  mas yr $^{-1}$  with a FWHM of  $\sim 12$  mas yr $^{-1}$ . Both the R.A. and decl. distributions are asymmetrical, and their FWHMs are a factor of  $\gtrsim 3\sigma$  of the null pseudo-proper motions of BLAGNs.

We conclude that the recovery of the null proper motions of BLAGNs (whose distribution peaks at zero within the uncertainties) and the fact that these uncertainties are comparable to those from our other methods (Sections 6.1 and 6.2) show the robustness of our method of JSP proper-motion estimation.

## 7. Obtaining Stellar Space Velocities in the Galaxy from JSP Proper Motions and Empirically Derived Distances

In order to derive space velocities of the stars in our sample, also using estimates of their distances to the Earth, their proper motions need to be corrected for the effects caused by the motion of the solar system relative to the LSR. This motion is in the apparent “apex” direction,  $R.A._{\text{apex}} = 277.0^\circ$ ,  $decl._{\text{apex}} = 30.0^\circ$ , at a speed  $S_\odot \sim 16$  km s $^{-1}$ . The effect of the solar motion on measured proper motions is to impart a component

of motion that is maximal at sources located in a direction perpendicular to the above apex. This spurious component is in a direction away from the apex, along a “meridian” in a fictitious celestial coordinate system where the “north pole” is at the apex. Mihalas & Binney (1981) explained that the spurious component of motion has a speed of  $\pi S_\odot \sin(\gamma)/4.74$ , where  $\gamma$  is the great-circle angular distance between the north pole or apex and the source, and  $\pi$  is its parallax in arcseconds.

The parallax of sources was obtained from the Gaia DR2 catalog or an empirical relation between parallax and total proper motion derived from Gaia DR2 matched sources. Figure 12 shows the Gaia DR2 parallax of 3367 sources with positive values (indicating valid Gaia DR2 solutions), out of the 3937 Gaia matches to ACS sources, as a function of total Gaia DR2 proper motion (quadrature combination of the R.A. and decl. components).

From Figure 12, we derived the following provisional empirical relation:

$$\begin{aligned} \pi_{\text{empirical}} = & 0.558657 + 0.0240032\mu_{\text{total}} \\ & + 0.00157145\mu_{\text{total}}^2 - 3.68780 \times 10^{-5}\mu_{\text{total}}^3 + 3.39325 \times 10^{-7}\mu_{\text{total}}^4. \end{aligned} \quad (2)$$

A drawback of Equation (2) is that it is based on a mixture of luminosity classes and spectral types in the sample of 3367 stars. In order to improve it, we first obtained the colors of stars in the  $r$  and  $i^+$  Subaru Suprime-Cam bandpasses (centered at wavelengths of 6288 and 7683.9 Å, respectively) from the COSMOS 2015 catalog (Laigle et al. 2016). These bandpasses were chosen because they were obtained in a homogeneous survey, and their depths are comparable (26.5 and 26.2 mag, respectively). The color excess  $E(B - V)$  for all stars that we considered in the COSMOS field was obtained from Laigle et al. (2016) and was in the range 0.0158–0.0243 mag. The extinction law was taken as  $2.660E(B - V)$  in the  $r$  filter and  $1.991E(B - V)$  in the  $i^+$  filter (Laigle et al. 2016, and references therein) and applied to deredden all of the stars in our sample. We generated synthetic  $r - i^+$  colors of main-sequence, giant, and supergiant stars by convolving either empirical templates of main-sequence and giant stellar spectra (Kesseli et al. 2017) or Kurucz–Lejeune model spectra of supergiants (Lejeune et al. 1997), with the transmission functions of the  $r$  and  $i^+$  filters from Taniguchi et al. (2007, 2015) and Laigle et al. (2016). We then compared the observed  $r - i^+$  colors of the stars with the above synthetic colors to assign a spectral type to each.

We established relations between Gaia DR2 parallax and total proper motion analogous to Equation (2) but restricting stars in the sample within narrow ranges of spectral type and luminosity class. The reason for selecting these narrow ranges was to minimize the effects of varying intrinsic brightness on inferred parallaxes when later applying these relations to non-Gaia stars. Early-type, young stars are expected to be located at smaller Galactic scale heights than late-type, older stars. However, excursions in the Galactic space velocities of stars, and therefore on their proper motions, are expected because of variations in the progenitor initial velocities even among stars formed at common locations, and later on during the life cycles of stars because of stellar encounters. These effects introduce large errors when applying these relations to individual sources. Caution is a must if trying to obtain individual source empirical parallaxes when applying the relations to non-Gaia stars. The

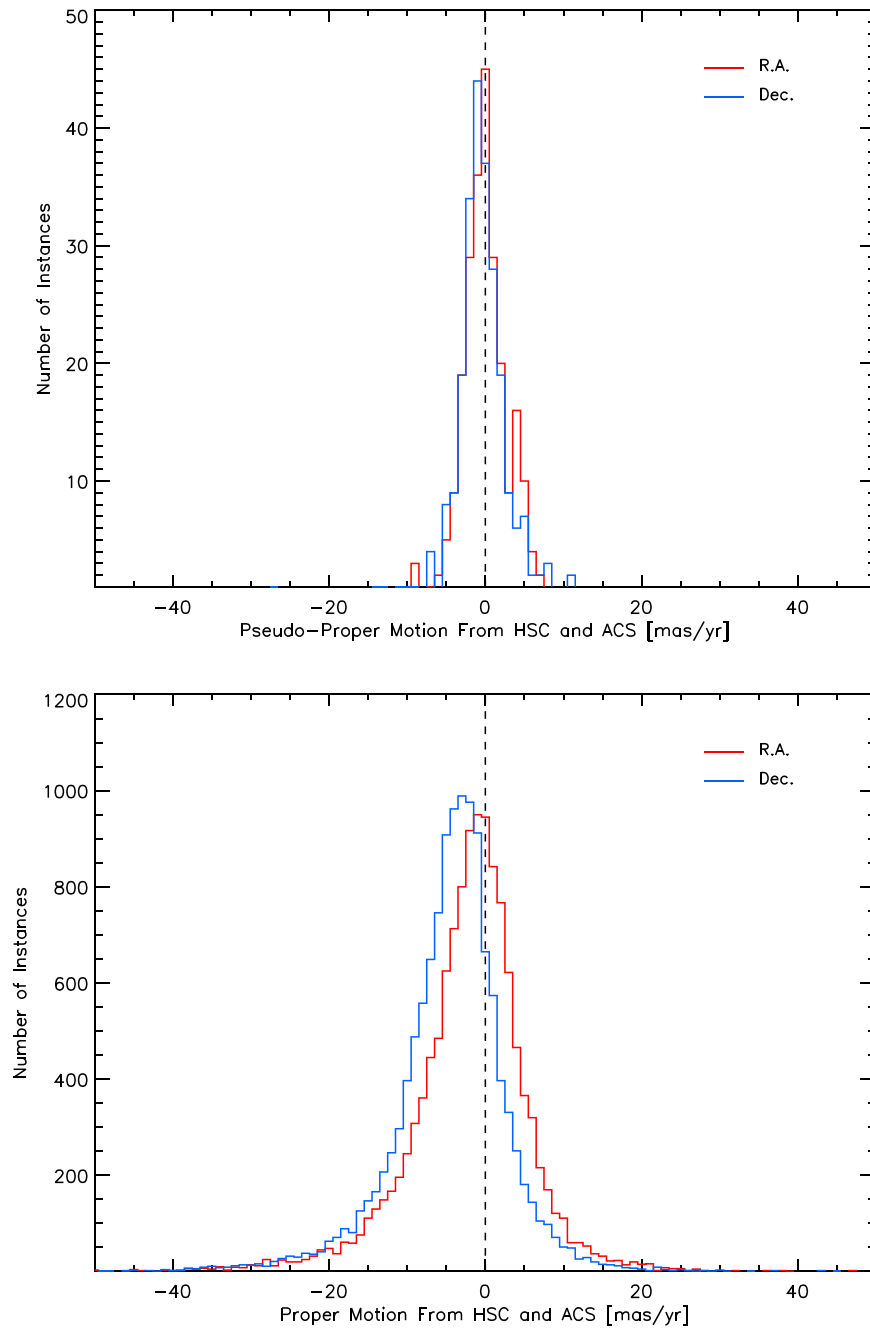


**Figure 11.** (a) Histogram of JSP pseudo-proper motions of 296 BLAGNs, explained in the text. The red line is for R.A. pseudo-proper motions, and the blue line is for decl. ones, both of which expected to be statistically null. The vertical dashed line denotes zero proper motions. (b) Histogram of the JSP proper motions of 12,529 stars, drawn from Gaia DR2 (Section 4.1) or empirically selected faint stars (Section 5). The lines are the same as in panel (a).

relations are instead meant to obtain mean proper motions of ensembles of stars, as described in this section.

We selected Gaia DR2 stars within the color intervals shown in Figure 13, which is a histogram of Gaia-ACS matches in these intervals. The photometric uncertainty in each of the  $r$  and  $i^+$  bands was required to be  $<20\%$  in the COSMOS 2015 survey (Laigle et al. 2016).

For each Gaia-ACS match with a positive Gaia DR2 parallax, we first computed its absolute  $I$ -band magnitude assuming each of the luminosity classes (main sequence, giant, or supergiant) via the distance modulus obtained from its Gaia parallax and SExtractor ACS F814W magnitude. The absolute magnitudes  $M_I$  as a function of spectral type were obtained

from the online tabular compilation<sup>6</sup> (referred to by Pecaut & Mamajek 2013) for main-sequence stars, Mikami & Heck (1982) for giant stars, and Keenan & Pitts (1985) and Martins et al. (2005) for supergiant stars. Solar metallicity was assumed in the calculation of  $M_I$ . The luminosity class that yielded the closest match to the apparent magnitude in the F814W ACS bandpass was selected as the luminosity class for the star. Then, stars were grouped by  $r - i^+$  color and main-sequence, giant, and supergiant luminosity class in order to plot and fit a linear relation (or a slow-varying quadratic in a few cases) to the Gaia parallax versus total proper motion relation for constant

<sup>6</sup> See <http://www.pas.rochester.edu/~emamajek>.

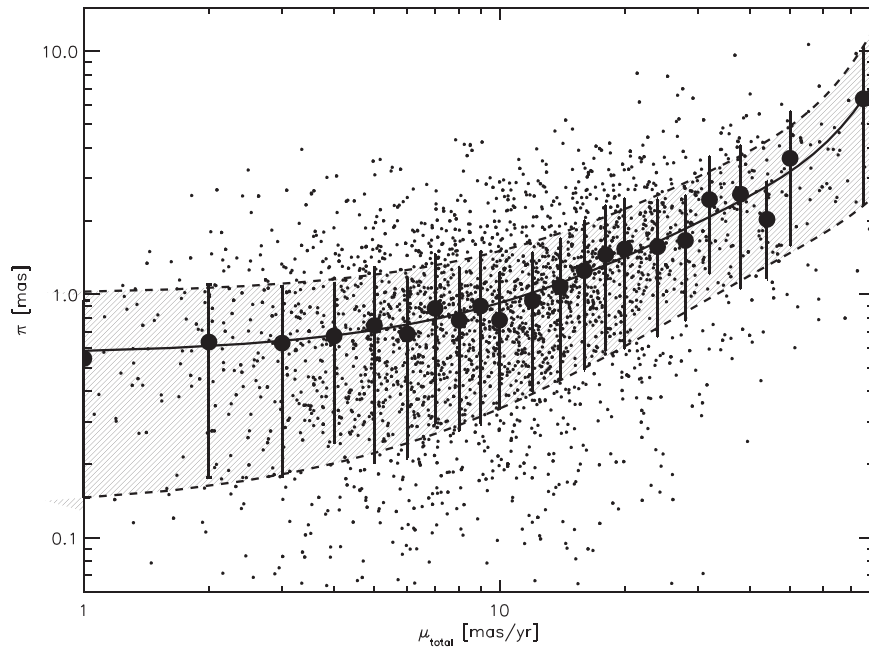


**Figure 12.** Gaia DR2 catalog parallax ( $\pi$ ) as a function of total proper motion ( $\mu_{\text{total}}$ ) for 3367 stars matched to ACS and with parallaxes  $>0$ , indicating valid Gaia DR2 solutions. The small black symbols correspond to individual stars. The large symbols with error bars are the proper motion–binned means and standard deviations of parallax. The solid line is a smoothed fourth-order polynomial, described in the text (Equation (2)) and fitted to the average parallax values, and the dashed lines are similar fits to the  $\pm 1$  standard deviation values, which bound the shaded region.

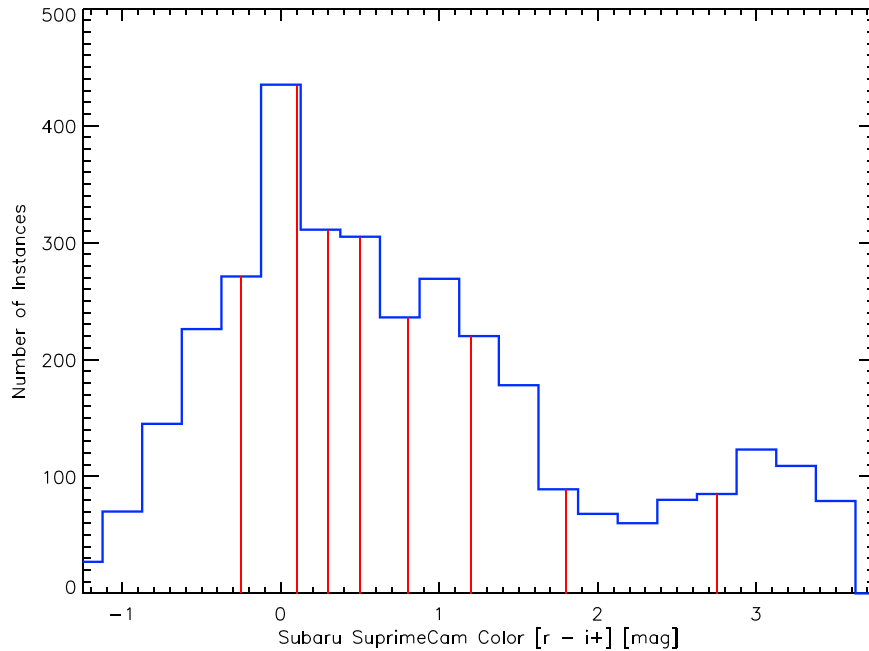


**Figure 13.** The blue line is the histogram of Subaru Suprime-Cam  $r - i^+$  colors of 3386 Gaia DR2–ACS matches in the color interval  $-1.25 < r - i^+ < 3.75$ , which encompasses normal stars. The vertical red lines denote the boundaries of the  $r - i^+$  color groups we used in Section 7 as a proxy for narrow ranges of spectral types (listed in Table 1).

luminosity class and within a narrow range of spectral types. Figure 14 shows the Gaia DR2 parallax versus total proper motion for main-sequence stars of color  $0.8 \text{ mag} < r - i^+ < 1.2 \text{ mag}$  or, per Table 1, spectral type M2–M3. Similar relations of parallax as a function of total proper motion were established for main-sequence and giant stars in groups of  $r - i^+$  colors or approximate spectral types listed in Table 1 (whenever there were sufficient stars). This table also

lists the linear or, in a few cases, quadratic fit parameters for the above relations. There were not sufficient supergiant stars to establish a relation.

For comparison, we also obtained relations between Gaia DR2 parallax and total proper motion analogous to those in Table 1 but for all Gaia DR2 parallaxes, regardless of whether they were positive or negative. We find that the y-intercept  $a_0$  of the relations is typically  $\sim 20\%–65\%$  of those in Table 1, the

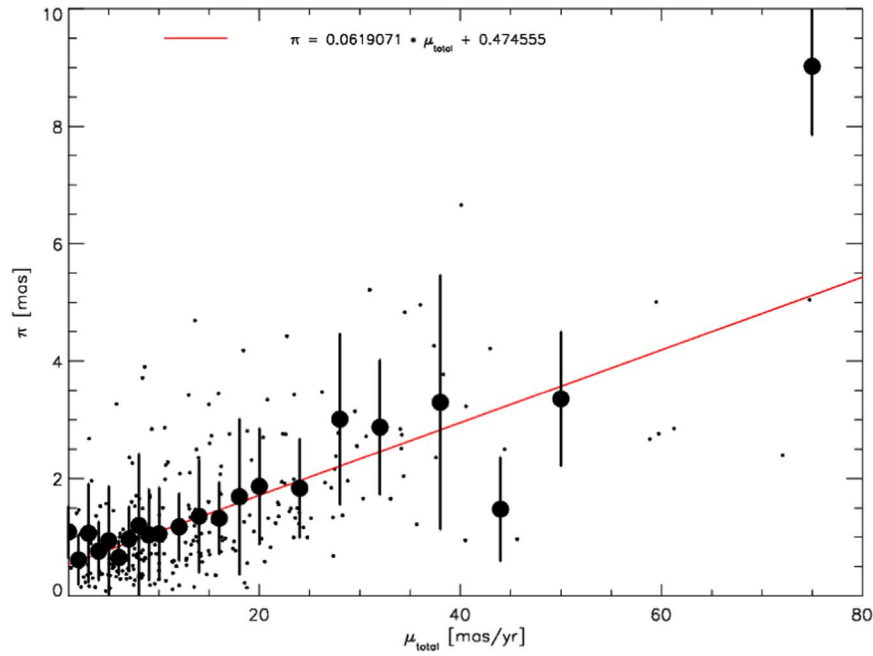


**Figure 14.** Gaia DR2 catalog parallax as a function of total proper motion for early M-type main-sequence Gaia DR2–ACS matched stars (whose luminosity class and spectral type were determined as described in the text, with colors in the interval  $0.8 < r - i^+ < 1.2$ ) and with parallaxes  $>0$ . The small black symbols correspond to individual stars. The large symbols with error bars are the proper motion–binned means and standard deviations of parallax. The solid red line is a fit to the proper motion–binned means.

**Table 1**  
Polynomial Fits to the Relation of Gaia DR2 Parallax as a Function of Total Proper Motion, Color, and Luminosity Class<sup>a</sup>

Color $r - i^+$	Spectral Type	$a_0$	$a_1$	$a_2$
<b>Main-sequence Stars</b>				
–1.25 to –0.25	O4 to B6	$0.446 \pm 0.032$	$0.0418 \pm 0.0028$	...
–0.25 to 0.10	B7 to G0	$0.708 \pm 0.042$	$0.0325 \pm 0.0034$	...
0.10 to 0.30	G1 to K3	$0.640 \pm 0.047$	$0.0406 \pm 0.0040$	...
0.30 to 0.50	K4 to K7	$1.012 \pm 0.139$	$0.0273 \pm 0.0052$	...
0.50 to 0.80	K8 to M1	$0.481 \pm 0.143$	$0.0585 \pm 0.0054$	...
0.80 to 1.20	M2 to M3	$0.474 \pm 0.048$	$0.0619 \pm 0.0034$	...
1.20 to 1.80	M4 to M5	$0.502 \pm 0.151$	$0.0541 \pm 0.0058$	...
1.80 to 2.75	M6 to M8	$0.891 \pm 0.182$	$-0.00645 \pm 0.0157$	$0.00184 \pm 0.00023$
2.75 to 3.75	M8 to L0	$1.064 \pm 0.206$	$-0.0053 \pm 0.0236$	$0.00062 \pm 0.00048$
<b>Giant Stars</b>				
0.50 to 0.80	K8 to M1	$0.0102 \pm 0.391$	$0.00699 \pm 0.00531$	...
0.80 to 1.20	M2 to M3	$0.0209 \pm 0.0958$	$0.0051 \pm 0.0102$	...
1.20 to 1.80	M4 to M5	$0.0559 \pm 0.0154$	$0.0027 \pm 0.0030$	...
1.80 to 2.75	Mid-to-late M	$0.150 \pm 0.099$	$0.0194 \pm 0.0097$	...
2.75 to 3.75	Late M	$0.180 \pm 0.026$	$0.0040 \pm 0.0039$	...

**Note.**

<sup>a</sup> Polynomial fits to the relation of Gaia DR2 parallax as a function of total proper motion, as well as a function of Subaru Suprime-Cam color  $r - i^+$  and luminosity class (main-sequence or giant stars). These relations were established from 2703 stars with positive Gaia DR2 parallax, colors in the interval  $-1.25 \text{ mag} < r - i^+ < 3.75 \text{ mag}$ , and photometric uncertainties  $<20\%$  in the  $r$  and  $i^+$  bandpasses. The relations are  $\pi = a_0 + a_1 \mu_{\text{total}}$  if only  $a_0$  and  $a_1$  are listed and  $\pi = a_0 + a_1 \mu_{\text{total}} + a_2 \mu_{\text{total}}^2$  if  $a_0$ ,  $a_1$ , and  $a_2$  are listed. The quoted errors in the linear or quadratic fit coefficients are  $\pm 1$  standard deviation.

slope is  $\sim 10\%$ – $48\%$  steeper, and the uncertainties in the parameters  $a_0$ ,  $a_1$ , and  $a_2$  are  $\sim 10\%$ – $20\%$  larger than in Table 1. Later in this section, we quantify the effect of applying these relations to the statistics of proper motions of non-Gaia stars.

We attempted to derive parallaxes among the 11,519 empirically selected faint stars (matched in ACS and HSC). Of these, 10,818 had COSMOS 2015 Subaru Suprime-Cam colors in the interval  $-1.25 \text{ mag} < r - i^+ < 3.75 \text{ mag}$  and

photometric uncertainties  $<20\%$  in the  $r$  and  $i^+$  bandpasses. The relations of Table 1 were separately applied for main-sequence, giant, and supergiant stars, since we did not know a priori the luminosity class of these sources. The distance modulus and absolute magnitudes in the  $I$  band were computed for each of these three luminosity classes from the corresponding empirical parallax. The luminosity class was identified by finding the closest match of apparent magnitude in the HSC  $i$  band and from the distance modulus. Among these sources,

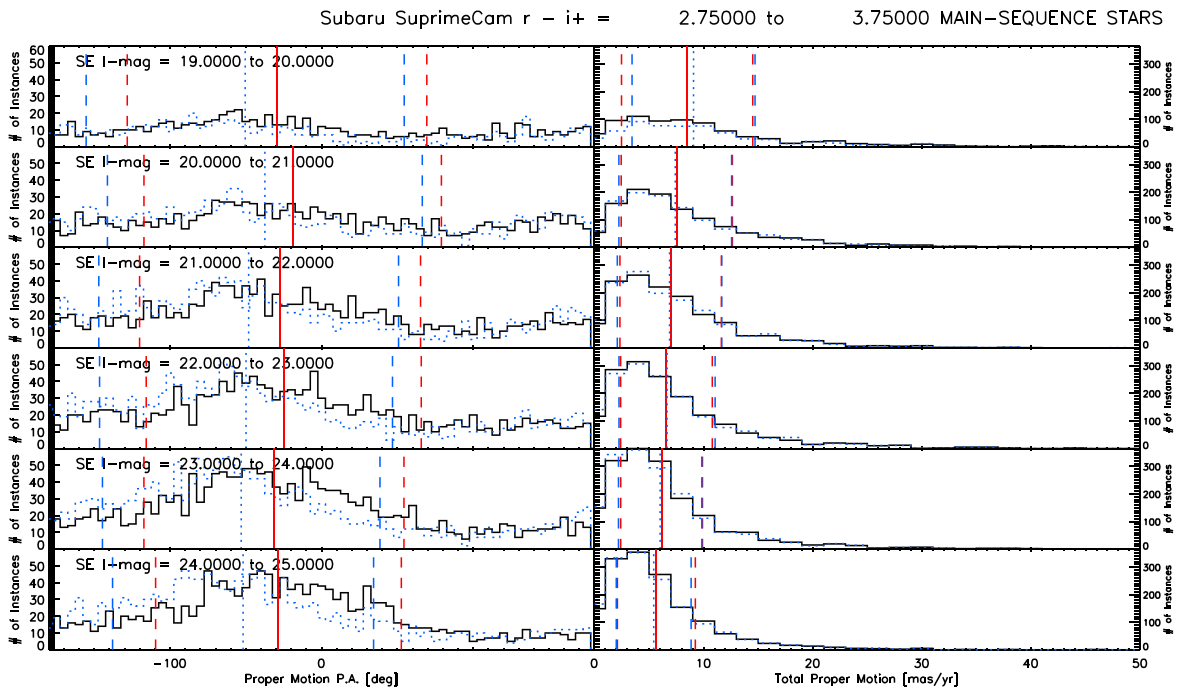


**Figure 15.** The solid black lines are histograms of proper-motion vectors of 8506 late-type (M8–9) main-sequence stars with Subaru Suprime-Cam  $r - i^+$  colors in the range 2.75–3.75 mag and SExtractor AB 19–25 mag. The left panels are histograms of position angle, defined here as  $0^\circ$  due E,  $90^\circ$  due N, and  $-90^\circ$  due S. The right panels are histograms of magnitude (quadrature combination of R.A. and decl. components). Each row corresponds to a bin of SExtractor AB mag. The red solid vertical line in each bin is the  $3\sigma$ -clipped mean, and the red dashed vertical lines denote the  $\pm 3\sigma$ -clipped standard deviation. For comparison with the above, using an astrometric grid of all Gaia stars, regardless of whether their parallaxes were positive or negative, the blue dotted lines are analogous histograms, and the blue vertical dotted and dashed lines denote the analogous  $3\sigma$ -clipped mean and  $\pm 3\sigma$ -clipped standard deviation, respectively.

we determined that 10,816 are main-sequence stars, and two are giant stars. No supergiants were identified in the sample. With the identified luminosity class and corresponding parallax for each of these sources, we obtained and subtracted the spurious component of proper motion due to the solar motion relative to the LSR.

After applying the correction of proper motions for the effect of the intrinsic motion of the solar system, described above, we obtained the proper motions of 10,818 empirically selected faint stars and 1010 Gaia–ACS stars exclusive of the empirically selected ones. In Figure 15, we show histograms of the proper motions of 8506 late-type main-sequence stars, comprised of 8358 empirically selected faint stars and 148 Gaia–ACS stars with  $r - i^+$  colors in the range 2.75–3.75 mag and an apparent AB mag between 19 and 25. The empirically derived parallaxes of these sources are in the range 1.05–2.37 mas with a mean of 1.09 mas or a range of distances 421–950 pc with a mean of 915 pc. The median proper motion of these sources is predominantly in the ESE direction, or at a so-called “position angle” of  $-30^\circ$ , as shown in Figure 15, and defined as  $0^\circ$  due E and  $90^\circ$  due N. Figure 15 also shows, as dotted blue lines, similar histograms of the position angle and vector magnitude of proper motion of the same sources but after using all Gaia DR2 sources for astrometric correction and empirical parallax estimation, regardless of whether their parallaxes were positive or negative. The histograms are very similar to those using only positive Gaia parallaxes; the mean position angle is  $-50^\circ$  and does not alter our conclusions. The mean vector magnitude of proper motion is essentially unchanged. Table 2 lists the mean and standard deviation of proper motions for the 10,818 empirically selected faint main-sequence and giant stars in bins of  $r - i^+$  color and SExtractor ACS F814W magnitude. The bins listed in Table 2 were meant

to contain stars of narrow ranges in not only spectral type and constant luminosity class but also apparent brightness. These bins do not necessarily translate into bins of constant parallax or distance to the Earth due to dispersion in individual stellar velocities, as explained earlier in this section. However, the mean distance to Earth was expected to follow an increasing trend for fainter bins within each spectral type and luminosity class bin. Our objective was to probe any pattern in mean proper motions in the COSMOS field as a function of distance to the Earth. Table 2 lets us identify bins with statistically significant median proper motions, such as those of late-type main-sequence stars plotted in Figure 15. Figure 15 shows that the mean proper motion varies from  $\sim 5.8 \text{ mas yr}^{-1}$  at the farthest distance of  $\sim 950 \text{ pc}$  to  $\sim 9 \text{ mas yr}^{-1}$  at the closest distance of  $\sim 421 \text{ pc}$ . Equivalently, Figure 15 also shows that the fraction of stars with proper motions  $> 10 \text{ mas yr}^{-1}$  out of the total number of stars in each bin varies from 16% at the farthest distance to 37% at the closest distance.

At the mean Galactic coordinates of the COSMOS field ( $236.6^\circ, +42.1^\circ$ ), the galactocentric Cartesian coordinates ( $x, y, z$ ) (each in kiloparsecs) are, as a function of distance  $D$  (kiloparsecs) to the Sun,

$$x = -0.406D - 8.2, \quad (3)$$

$$y = -0.621D, \quad (4)$$

$$z = +0.670D, \quad (5)$$

where  $x$  points from the Sun and is positive toward the Galactic center,  $y$  is parallel to the Galactic plane and positive in the Galactic rotation direction, and  $z$  is the vertical distance to the Galactic plane and positive toward the north Galactic pole, as described by, e.g., Yan et al. (2020). In this coordinate system, the Sun is located at  $(-8.2, 0, 0.015)$  (kpc).

**Table 2**  
Proper Motions in R.A. and decl. as a Function of Luminosity Class, Color, and SExtractor AB Magnitude<sup>a</sup>

Color $r - i^+$	SExtractor AB Magnitude					
	19–20	20–21	21–22	22–23	23–24	24–25
Main-sequence Stars						
–1.25 to –0.25	0.77 ± 1.41	–0.96 ± 1.07	–1.57 ± 0.71	0.95 ± 0.63	0.74 ± 0.67	1.68 ± 0.70
	–3.33 ± 1.57	–1.02 ± 0.56	–1.02 ± 0.55	–1.98 ± 0.56	–1.82 ± 0.76	–1.22 ± 0.81
–0.25 to +0.10	2.00 ± 2.60	–1.96 ± 1.91	0.41 ± 0.86	0.99 ± 0.66	1.06 ± 0.67	2.11 ± 0.66
	–0.64 ± 2.92	–4.30 ± 1.35	–3.05 ± 0.86	–1.74 ± 0.78	–0.65 ± 0.70	–1.34 ± 0.50
+0.10 to +0.30	2.11 ± 2.57	–1.56 ± 1.19	–0.65 ± 0.97	1.25 ± 1.01	0.97 ± 0.71	1.33 ± 0.79
	–5.59 ± 1.58	–2.52 ± 1.11	–2.45 ± 0.76	–1.52 ± 0.78	–1.52 ± 0.77	–1.64 ± 0.82
+0.30 to +0.50	–0.15 ± 1.32	1.42 ± 1.25	2.20 ± 1.22	0.93 ± 1.06	1.47 ± 0.74	3.89 ± 0.63
	–3.67 ± 1.47	–1.06 ± 0.94	–0.46 ± 1.09	–1.21 ± 0.81	–1.50 ± 0.64	–1.64 ± 0.88
+0.50 to +0.80	–0.12 ± 1.78	–1.12 ± 1.30	1.09 ± 0.82	0.87 ± 0.94	0.77 ± 0.63	2.34 ± 0.69
	–2.42 ± 1.86	–3.52 ± 0.98	–2.17 ± 0.77	–1.16 ± 0.83	–2.11 ± 0.46	–1.26 ± 0.61
+0.80 to +1.20	1.30 ± 1.94	1.29 ± 1.61	1.79 ± 0.69	–0.05 ± 0.98	0.41 ± 0.57	2.24 ± 0.59
	–0.17 ± 1.64	–1.05 ± 1.25	–0.55 ± 0.87	–2.02 ± 0.97	–2.62 ± 0.63	–0.63 ± 0.74
+1.20 to +1.80	–4.01 ± 0.88	–0.11 ± 1.01	–0.40 ± 0.61	1.97 ± 1.07	1.53 ± 0.60	2.02 ± 0.54
	–2.59 ± 1.29	–0.17 ± 0.99	–1.69 ± 0.67	–3.48 ± 0.94	–1.93 ± 0.40	–2.06 ± 0.54
+1.80 to +2.75	–3.27 ± 2.96	2.81 ± 1.43	3.39 ± 1.13	2.22 ± 0.74	2.37 ± 0.71	1.82 ± 0.61
	–0.04 ± 2.09	–3.19 ± 1.39	–0.44 ± 0.69	–1.46 ± 1.06	–0.82 ± 0.52	–0.66 ± 0.66
+2.75 to +3.75	0.87 ± 0.33	1.32 ± 0.22	1.64 ± 0.17	1.55 ± 0.16	2.13 ± 0.14	2.25 ± 0.13
	–1.93 ± 0.30	–0.92 ± 0.21	–1.57 ± 0.17	–1.36 ± 0.16	–1.50 ± 0.13	–1.34 ± 0.12
Giant Stars						
+0.50 to +0.80	...	...	0.39 ± 2.55	...	...	–0.28 ± 1.67
	...	...	0.07 ± 1.60	...	...	–0.48 ± 1.97

**Note.**

<sup>a</sup> Each table entry corresponds to a given  $r - i^+$  color range and SExtractor AB mag range separately for main-sequence and giant stars. In the case of main-sequence stars, each table entry lists the median  $\pm 3\sigma$ -clipped standard deviation of the mean of proper motion in R.A. (upper row of table entry) and decl. (lower row of table entry). In the case of giant stars, only two objects were identified in our sample of faint stars, and each belongs in a separate SExtractor AB magnitude range; thus, their proper motions are for individual objects, and their uncertainties are as calculated in Section 6.

Given proper motions  $\mu_\alpha$  (R.A.) and  $\mu_\delta$  (decl.) in milliarcseconds per year, radial velocity  $v_{\text{rad}}$  in kilometers per second (along the line of sight by definition), and distance  $D$  in kiloparsecs, Galactic space velocities ( $U$ ,  $V$ ,  $W$ ) relative to the LSR were calculated using the procedure by Johnson & Soderblom (1987), except that the velocity component  $U$ , parallel to the Galactic plane and pointing away from the Galactic center, is positive in this last sense. The velocity component  $V$  is also parallel to the Galactic plane and points in the direction of Galactic rotation, while  $W$  is perpendicular to the Galactic plane and is positive toward the north Galactic pole.

The faintest late-type main-sequence stars in Figure 15 (1540 stars with AB mag in the range 24–25) have mean proper motions  $\langle \mu_\alpha \rangle \sim 5.02$  and  $\langle \mu_\delta \rangle \sim -2.9$  mas yr<sup>–1</sup>, as derived from the bottom panels in Figure 15, and a mean parallax of  $\sim 1.07$  mas. For this group of stars, we calculated the  $U$ ,  $V$ , and  $W$  velocity components from their individual proper motions and parallaxes, assuming at first zero radial velocities, to get a range of components from  $-99$  to  $+81$  km s<sup>–1</sup>. We then used this range to estimate that  $v_{\text{rad}}$  can be, at most, in the range from  $\sim -80$  to  $+80$  km s<sup>–1</sup>. We then computed the  $U$ ,  $V$ , and  $W$  velocity components corresponding to the mean proper motion and parallax of these stars and assuming radial velocities in the above range. Figure 16 shows the resulting possible velocities corresponding to the mean proper motions and parallax and radial velocities from  $-80$  to  $+80$  km s<sup>–1</sup>.

From Figure 16, it can be seen that the rotational ( $V$ ) and vertical ( $W$ ) velocities are very nearly equal in magnitude and of opposite sign for any given radial velocity. They are  $\sim 0$  km s<sup>–1</sup> for a radial velocity of  $\sim -12$  km s<sup>–1</sup>. The velocity

component  $V$  does not dominate over the other components  $U$  and  $W$  for any radial velocity. Thus, the mean motion of these faint late-type main-sequence stars is not predominantly along the Galactic rotation. It is unlikely that the vertical velocity  $W$  is large, which would place limits on the extreme radial velocity. If  $-10$  km s<sup>–1</sup>  $< W < +10$  km s<sup>–1</sup>, then  $-30$  km s<sup>–1</sup>  $< v_{\text{rad}} < 0$  km s<sup>–1</sup>. The  $U$  velocity is  $< 0$  for most radial velocities. That is, the mean or predominant motion of late-type main-sequence stars at  $\sim 934$  pc is toward the Galactic center. In the range of radial velocities  $-30$  km s<sup>–1</sup>  $< v_{\text{rad}} < 0$  km s<sup>–1</sup>,  $U$  dominates over both  $V$  and  $W$  by a factor of at least  $\sim 2$ .

In order to estimate the membership of the 8358 empirically selected faint stars and 148 Gaia–ACS matched stars of late-type main-sequence classification in the thin and thick disks of the galaxy, we calculated lower limits (because of the absence of radial velocity information) to ( $U$ ,  $V$ ,  $W$ ) space velocities relative to the LSR for each of them. We then plotted a Toomre diagram, consisting of  $\sqrt{U^2 + W^2}$  as a function of  $V$  (Toomre 1964; Yan et al. 2020). We distinguished stars in the thin disk, thick disk, and halo based on whether the total velocity  $v_{\text{tot}} = \sqrt{U^2 + V^2 + W^2}$  is, respectively,  $v_{\text{tot}} < 85$  km s<sup>–1</sup>,  $85$  km s<sup>–1</sup>  $< v_{\text{tot}} < 220$  km s<sup>–1</sup>, or  $v_{\text{tot}} > 220$  km s<sup>–1</sup> (Nissen 2004; Venn et al. 2004; Yan et al. 2020). The Toomre diagram of these stars is shown in Figure 17(a), where it can be seen that the majority of these stars are in the thin disk. The delimited “fanlike” appearance of the locus of these stars is due to the fact that the radial velocity  $v_{\text{rad}}$  has been assumed to be zero. The inclusion of nonzero  $v_{\text{rad}}$  would not alter our conclusion that most stars have  $v_{\text{tot}} < 85$  km s<sup>–1</sup> for most values of  $v_{\text{rad}}$ , as suggested by the dashed line in Figure 16, and

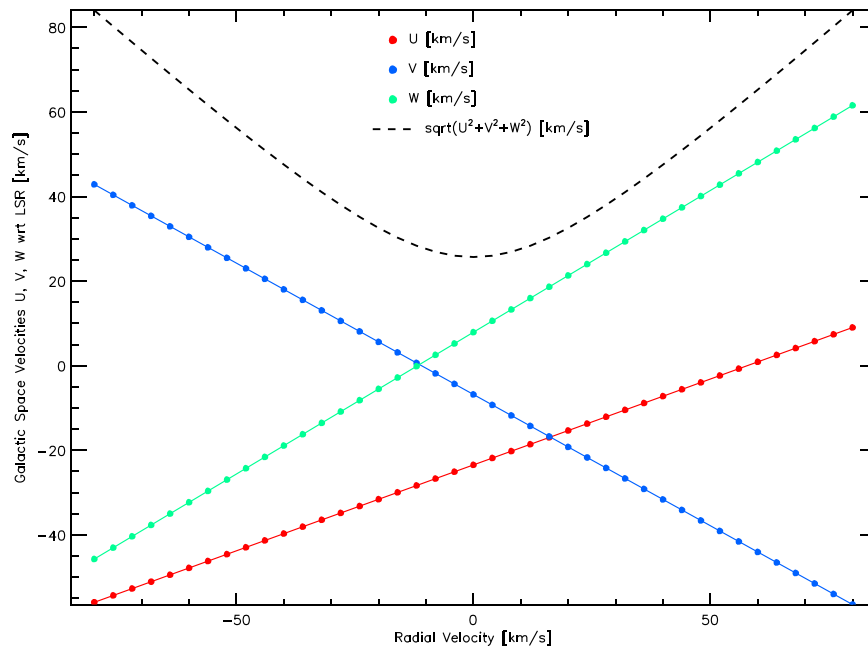


**Figure 16.** Galactic space velocity components  $U$ ,  $V$ , and  $W$  for late-type main-sequence stars with Subaru Suprime-Cam colors  $2.75 < r - i^+ < 3.75$  and SExtractor F814W AB magnitude in the range 24–25. The  $(U, V, W)$  velocities were computed from a mean proper motion of  $5.8 \text{ mas yr}^{-1}$  directed  $-30^\circ$  (clockwise) from E, as obtained from 1540 stars whose histograms of proper motions are shown in the bottom panel of Figure 15. The mean parallax for these stars of  $1.07 \text{ mas}$  was also assumed, and radial velocities were varied from  $-80$  to  $+80 \text{ km s}^{-1}$ . The red symbols are the  $U$  velocities, the blue symbols are the  $V$  velocities, the green symbols are the  $W$  velocities, and the black dashed line denotes the total velocities.

the fact that there are many fewer stars with  $v_{\text{tot}}$  at or near the thin disk limit of  $85 \text{ km s}^{-1}$  in Figure 17(a).

We next searched for any candidate high-velocity stars belonging to the halo in the whole sample of stars with JSP proper motions in the COSMOS field. The sample of late-type main-sequence stars plotted in Figure 17(a) does not include any such halo members. Figure 17(b) is the Toomre diagram of all 11,828 stars, of which 10,818 are from our empirically selected faint star sample, and 1010 are from Gaia–ACS matches with Subaru Suprime-Cam colors  $-1.25 < r - i^+ < 3.75$  and SExtractor AB mag in the F814W ACS filter between 19 and 25 for which empirical parallaxes, spectral types, and luminosity classes could be derived. Figure 17(b) shows that two sources, shown as large black filled circles, are candidate high-velocity stars in the Galactic halo. The first two rows of Table 3 list these two sources. It should be recalled that the derivation of the empirical parallaxes needed to derive the space velocities in Figures 17(a) and (b) assumed solar metallicity, as described earlier in this section. We rederived the empirical parallaxes and distances to these two sources by assuming metal-poor giant star absolute magnitudes at the Galactic halo. For this purpose, we used the Dartmouth Stellar Evolution Program (DSEP) database<sup>7</sup> (Dotter et al. 2008) and selected an isochrone for an age of 13 Gyr, metallicity of  $[\text{Fe}/\text{H}] = -2.0 \text{ dex}$  and  $[\alpha/\text{Fe}] = -0.2 \text{ dex}$ , and bandpasses in the SDSS *ugirz* photometric system. The Subaru Suprime-Cam  $r - i^+$  and SDSS  $r - i$  colors are very similar, as we confirmed by comparing our synthetic colors of main-sequence and giant stellar spectra by Kesseli et al. (2017) and corresponding SDSS colors for the same spectra (op cit). By comparing the above metal-poor isochrone with the corresponding solar metallicity one, it is seen that metal-poor giants are more luminous than solar metallicity ones. In particular, K8- and M0-type metal-poor giants would

be factors of  $\sim 6.6$  and  $6.1$ , respectively, farther away than solar metallicity ones for a constant apparent  $i$  magnitude. We also rederived the empirical parallaxes or distances to these two stars by performing Monte Carlo simulations of distance, as explained in Appendix B. The errors in parallax of these distant stars and the Gaia DR2 stars used to derive the relations in Table 1 for giants are very large, as described in Appendix B. Therefore, a straightforward application of the relations for giants in Table 1, as carried out to generate the space velocities shown as large black filled circles in Figure 17(b), was deemed inexact. Instead, the application of the Monte Carlo simulations of distance resulted in the median distance and asymmetric upper and lower uncertainties listed in the first two rows of Table 3. Corresponding rederived Galactic space velocities for these two sources are shown in Figure 17 as blue solid lines representing the ranges of distances per the upper and lower uncertainties in Table 3. The uncertainties of the space velocities of these two giant stars are large, but candidate halo membership is possible.

We computed distances from Gaia DR2 parallaxes for the five K8–M1 giant stars that were used to generate the relation between Gaia parallax and total proper motion listed in Table 1 and whose data are plotted in the upper left panel of Figure 21. That is, we attempted to find out if these sources were themselves candidate high-velocity and/or candidate members of the Sangarius stream. These stars were drawn from among the 3937 Gaia–ACS matched sources, which are unconstrained in apparent magnitude and therefore were not previously analyzed because they were brighter than SExtractor F814W 18.5 mag. The relative uncertainties of the Gaia parallax for these sources are large; therefore, we performed Monte Carlo simulations of the parallax using 500 Gaussian deviates to estimate median distances and upper and lower asymmetric uncertainties, in analogy to Appendix B; see Luri et al. (2018). Of these five K8–M1 giant stars, three had distances smaller than 4 kpc and were discarded from our sample. The

<sup>7</sup> <http://stellar.dartmouth.edu/models/grid.html>

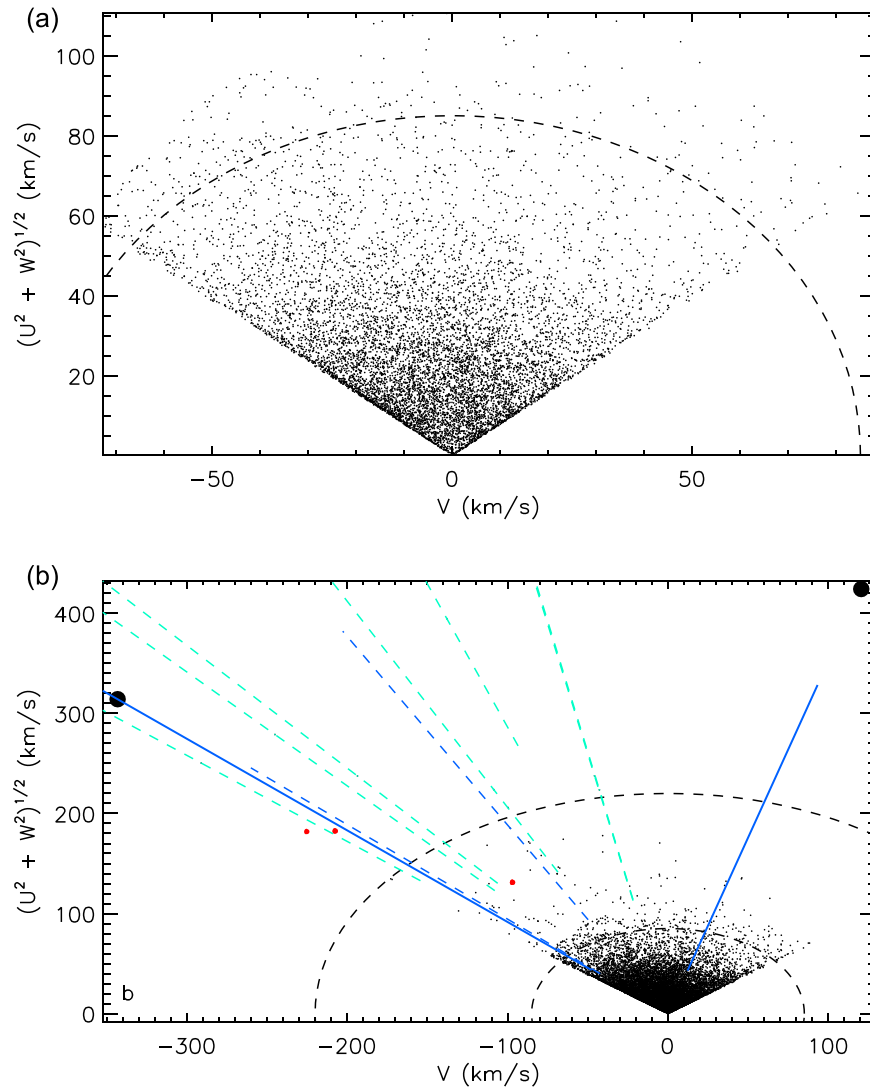


**Figure 17.** (a) Toomre diagram of 8506 late-type main-sequence stars comprised of 8358 empirically selected stars and 148 Gaia-ACS matches with Subaru Suprime-Cam colors  $2.75 < r - i^+ < 3.75$  and SExtractor F814W AB magnitude in the range 19–25. The dashed line denotes total velocity  $v_{\text{tot}} = 85 \text{ km s}^{-1}$  separating the thin and thick disk components of the galaxy. Dots denote the velocity components of each source. (b) Toomre diagram of 11,830 stars, comprised of 10,818 from our sample of empirically selected stars; 1010 from Gaia DR2-ACS matches with Subaru Suprime-Cam colors  $-1.25 < r - i^+ < 3.75$  and SExtractor F814W AB magnitude in the range 19–25, of which the sources in panel (a) are a subset; and two Gaia DR2-ACS matches as above but with SExtractor F814W AB mag  $< 18.5$ . The black dashed lines represent  $v_{\text{tot}}$  of 220 and  $85 \text{ km s}^{-1}$  to delimit the loci of the halo and of the thick and thin disks, respectively. The large filled circles denote initial estimates of the space velocities of two stars listed in the first two rows of Table 3, assuming solar metallicity giant star absolute magnitudes, that we estimate to be candidate members of the halo. The blue solid lines are rederived space velocities of these two stars assuming metal-poor giant star absolute magnitudes for consistency with the halo, as explained in the text, and also using Monte Carlo simulations in view of large parallax uncertainties, described in Appendix B, yielding distance and corresponding velocity ranges for each star. The small red filled circles are rederived space velocities of three metal-poor giant stars assumed to be at a distance of 20 kpc and listed in the third through fifth rows of Table 3. The blue and green dashed lines are ranges of space velocities for Gaia-ACS matched sources consisting, respectively, of two bright (SExtractor F814W AB mag  $< 18.5$ ) giant stars from the sample in the upper left panel of Figure 21 and six Gaia stars not in the sample of empirically selected faint stars. The two bright giant stars are at distances possibly consistent with 20 kpc at the Sangarius stream, but they are inconsistent with the metal-poor environment in this stream. They are listed in the sixth and seventh rows of Table 3. The six Gaia stars not in the empirical faint star sample are candidate high-velocity stars but at relatively near distances, as explained in the text. The parallaxes of the above eight sources from Gaia DR2 had large relative uncertainties; therefore, we derived ranges of distance and corresponding velocity using Monte Carlo simulations analogous to those in Appendix B (see also Luri et al. 2018).

remaining two sources are listed in the last two rows of Table 3, and their space velocities are shown as statistical ranges in Figure 17(b) as blue dashed lines.

Figure 17(b) shows that six stars from the sample of 1010 Gaia-ACS matches exclusive of empirically selected faint stars are candidate high-velocity objects. The relative uncertainties of the Gaia DR2 parallax were  $> 0.2$  for these objects. Therefore, to estimate their distances, we performed Monte Carlo simulations analogous to that shown in Appendix B, for consistency with Luri et al. (2018). Table 6 in Appendix C lists

the coordinates, median distances, and upper and lower asymmetric uncertainties of the distances of these six stars. It can be seen that their distances range from  $\sim 480$  to  $\sim 6170$  pc and therefore that they are relatively nearby. These candidate high-velocity stars are not further analyzed here, but the reader is referred to Table 6 for follow-up.

## 8. Discussion

To investigate whether the two giant stars in the first two rows of Table 3 are candidate members of the Sangarius

**Table 3**  
Candidate High-velocity Stars in the JSP Proper-motion Sample

R.A. (J2000.0)	Decl. (J2000)	JSP Proper Motions <sup>a</sup>		ACS F814W	Color $r - i$ <sup>b</sup>	Spectral Type <sup>c</sup>	Luminosity Class <sup>c</sup>	Distance <sup>d</sup>
		$\mu_\alpha$ mas yr <sup>-1</sup>	$\mu_\delta$ mas yr <sup>-1</sup>					
09 58 09.73415	+02 17 57.0692	+0.39 ± 2.55	+0.07 ± 1.60	21.738	0.6110 ± 0.0051	M0	III	54 <sup>+129</sup> <sub>-30</sub>
10 02 30.70664	+01 54 41.5045	-0.28 ± 1.67	-0.48 ± 1.97	24.735	0.529 ± 0.018	K8	III	59 <sup>+156</sup> <sub>-35</sub>
Candidates from Color–Magnitude Diagram <sup>e</sup>								
09 57 58.90735	+02 03 48.5148	+0.88 ± 1.93	-1.48 ± 1.72	19.418	0.108 ± 0.016	F9	III	...
09 58 10.82833	+02 02 21.8468	-0.79 ± 0.87	-2.95 ± 0.92	19.056	0.1162 ± 0.0036	F9	III	...
09 58 18.41377	+02 31 42.3111	+0.38 ± 0.73	-2.89 ± 2.31	20.025	0.1004 ± 0.0036	F9	III	...
Questionable Sources from Bright Gaia DR2 Solar Metallicity Stars <sup>f</sup>								
09 58 11.57578	+01 58 31.6744	-1.857 ± 0.067 <sup>g</sup>	-0.950 ± 0.068 <sup>g</sup>	15.780	0.7224 ± 0.0078	M1	III	21.2 <sup>+22.5</sup> <sub>-10.4</sub> <sup>f</sup>
10 01 20.02097	+02 01 05.3836	-1.68 ± 0.54 <sup>g</sup>	-2.68 ± 0.99 <sup>g</sup>	17.087	0.6945 ± 0.0061	M1	III	8.6 <sup>+15.3</sup> <sub>-4.7</sub> <sup>f</sup>

**Notes.**

<sup>a</sup> Corrected for the effect of solar motion, as explained in Section 7.

<sup>b</sup> Colors are from the Subaru Suprime-Cam COSMOS2015 survey (Laigle et al. 2016).

<sup>c</sup> Spectral types were derived from synthetic colors of main-sequence and giant stars using models from Kesseli et al. (2017), as explained in Section 7. Luminosity class was inferred from the observed SExtractor F814W AB magnitude and absolute magnitudes of main-sequence and giant stars (see references in Section 7).

<sup>d</sup> Starting from relations between Gaia proper motions and parallaxes, as explained in Section 7, Monte Carlo simulations of variations in these proper motions and parallaxes and in the JSP proper motion of the source itself were carried out to derive asymmetric distributions of simulated distance, as explained in Appendix B. In addition, the distance moduli used to compute empirical distances to these sources used metal-poor giant star absolute magnitudes, as explained in the text. For candidate sources from a color–magnitude diagram, where no data are shown, distances were assumed to be 20 kpc.

<sup>e</sup> Derived from a color–magnitude diagram for metal-poor giant stars at the distance to the Sangarius stream, as explained in Section 8.

<sup>f</sup> Sources are from the sample of K8–M1 giant stars from which a Gaia parallax versus total proper motion relation was established and applied to other sources (see the upper left panel of Figure 21 in Appendix B). In view of the large relative uncertainties of the Gaia parallaxes, Monte Carlo simulations of the parallax were carried out to derive asymmetric distributions of the simulated distance, analogous to the simulations in Appendix B; see also Luri et al. (2018). The classification of these sources as giants is based on solar metallicity models, explained in Section 7.

<sup>g</sup> Proper motions from the Gaia DR2 catalog, corrected for the effect of solar motion.

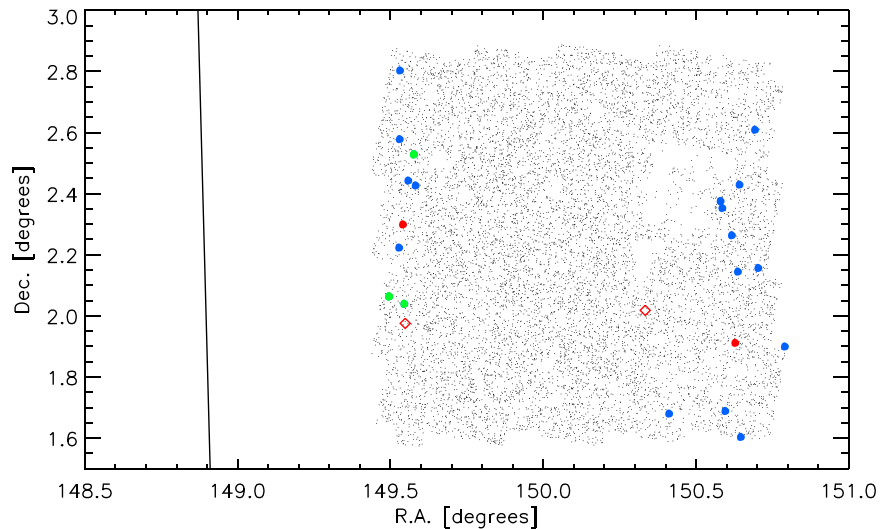


**Figure 18.** The dots are the coordinates of the sample of 10,818 stars with JSP proper motions, Subaru Suprime-Cam colors  $-1.25 < r - i^+ < 3.75$ , and SExtractor F814W AB magnitude in the range 19–25. The solid line delineates the center of the Sangarius stream (Grillmair 2017). The colored filled circles are the coordinates of 21 candidate Sangarius stream stars in our sample, of which the red circles are the two candidate high-velocity stars in the Toomre diagram in Figure 17(b), listed in the first two rows of Table 3, and the blue and green circles are the coordinates of 19 sources obtained from a color–magnitude diagram of metal-poor giant stars at the distance to the Sangarius stream. Of these 19 stars, the three stars whose coordinates are shown as green filled circles have proper motions consistent with the expected motions in the Sangarius stream, as further discussed in this section and Figure 19. The red open diamonds are the positions of two bright giant stars at distances similar to the Sangarius stream but of solar metallicity, which is inconsistent with the stellar population of this stream. These two stars are listed in the last two rows of Table 3 as questionable sources as regards candidate membership in Sangarius.

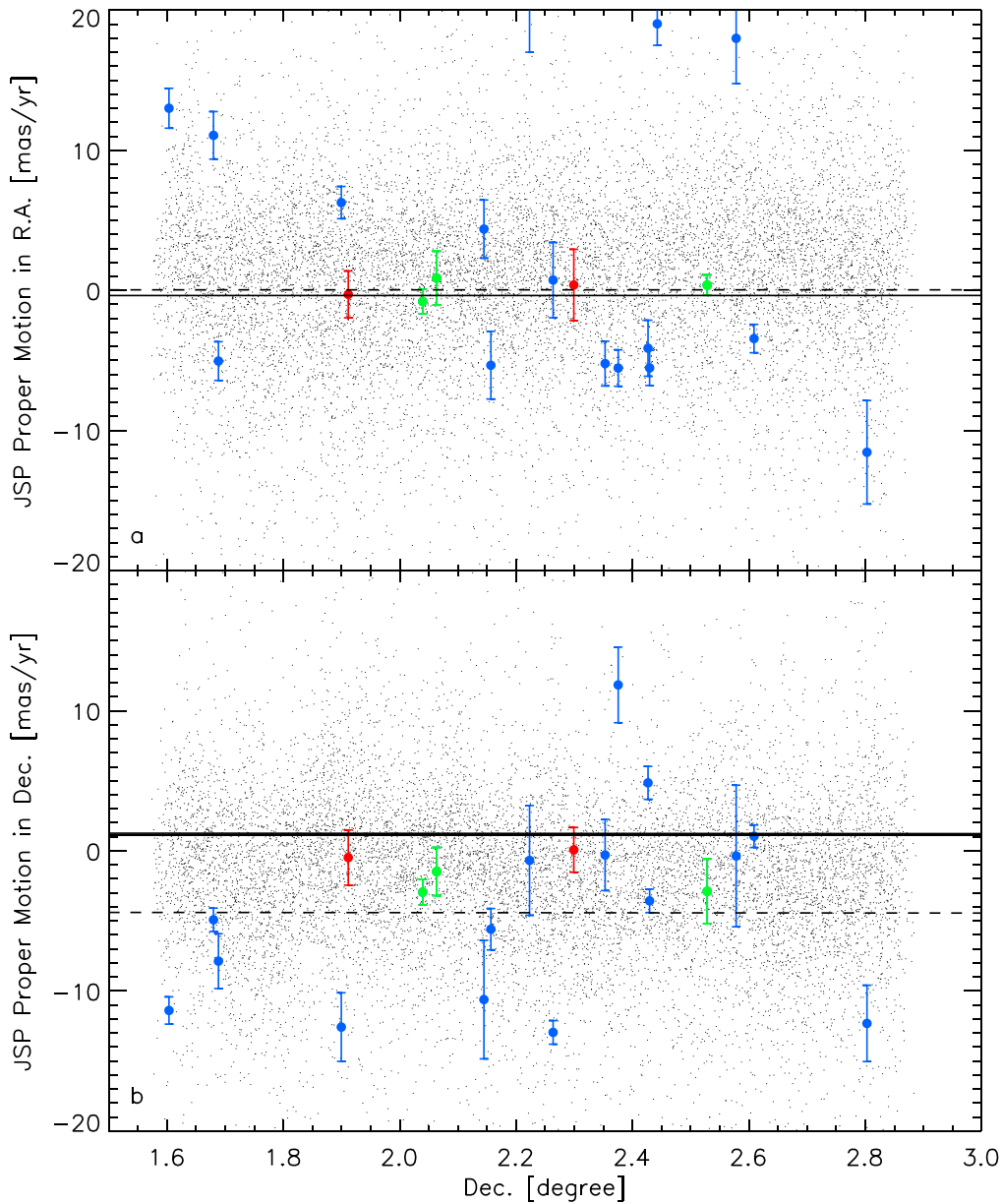
stream, which is a dynamically “cold” structure located at a distance of  $\sim 20$  kpc and extends for tens of degrees with a width of  $\sim 1^\circ$  (Grillmair 2017), we note that the stream passes  $\sim 0.5^\circ$  W of the COSMOS field as covered by ACS observations (Figure 18). It is possible that the eastern edge of the stream passes through the western edge of the COSMOS field. The positions of these two giant stars identified from proper motions and colors  $r - i^+$  are shown as red filled circles in Figure 18. Of these two stars, the M0 giant is located near the eastern edge of the Sangarius stream, and the K8 giant is located near the eastern edge of the COSMOS field. The lower limits of the distances to these two sources are  $\sim 24$  kpc (Table 3) and therefore suggest that membership in the Sangarius stream is possible.

Figure 18 also shows the positions of 19 stars from our sample, shown as blue and green filled circles, which were identified through the use of a color–magnitude diagram for metal-poor stars at the distance to the stream. In order to identify these 19 stars, we first used the DSEP (Dotter et al. 2008) metal-poor isochrone described above. We then assumed that all 10,818 empirical faint stars in our sample were at a distance of 20 kpc and computed their absolute AB mag in the SExtractor F814W bandpass from the corresponding distance modulus. In the resulting  $r - i^+$  color–SExtractor F814W absolute mag diagram of these sources, there were 19 stars whose absolute magnitude was within 1 mag of the above DSEP (Dotter et al. 2008) isochrone for giant stars. The relative uncertainty in  $r - i^+$  color was constrained to be less than 50% before selecting the above sources. Figure 18 shows that the 19 sources from the Sangarius-like metal-poor color–magnitude diagram and the above two giant stars (shown as red filled circles) fall in narrow bands in the COSMOS field along its western and eastern edges. It is possible that the band along the western edge of the COSMOS field consists of candidate members along the eastern edge of the Sangarius stream. The sources along the eastern boundary of the COSMOS field are

interesting; Grillmair (2017) found several more or less parallel N–S streams in the region he termed the Orphanage. However, the streams Scamander and PS1-D in this region are offset by  $\sim 8^\circ$  from Sangarius, far beyond the limits of the COSMOS field. It may be that the streams in the Orphanage are considerably more substructured than could be discerned from the limited resolution afforded by the much brighter magnitude limits of the SDSS and Pan-STARRS data. The band of sources at the eastern end of the COSMOS field is possibly a parallel splinter of the Sangarius stream and would add to the growing list of streams showing fibrous or banded structure, including the Anticenter stream and the Eastern Banded Structure (Grillmair 2006).

Of the 21 candidates shown in Figure 18 as filled circles, only three had counterparts in Gaia DR2 with Gaia parallaxes  $< 0$ . We visually inspected cutouts of the 21 sources in the HSC and ACS coadds to see if any of them were resolved galaxies or AGNs and if there were any edge effects that might have compromised their photometry or astrometry. All of the sources were pointlike, and they had no contamination or truncated edges within  $10''$ . In addition, we searched for X-ray counterparts for these 21 sources in the Chandra-COSMOS Legacy Survey Point Source Catalog (Civano et al. 2016; Marchesi et al. 2016) but found none within  $7''$ . Therefore, we believe none of these sources are unresolved AGNs.

Figure 18 also shows as red open diamonds the positions of two giant stars from the Gaia–ACS sample of 3939 stars that were unconstrained in SExtractor F814W AB mag. The two stars are brighter than AB 18.5 mag and thus not part of the sample of JSP sources because they are saturated in HSC and ACS. Their Gaia parallaxes suggest that they are at distances similar to the Sangarius stream. However, their classification as giant stars was based on solar metallicity models, which is inconsistent with the stellar population of the Sangarius stream. If the stars were metal-poor instead, they would be  $\sim 36$  times less luminous than giant



**Figure 19.** (a) The dots are the JSP proper motions in R.A. as a function of decl. for the 10,818 stars with Subaru Suprime-Cam colors  $-1.25 < r - i^+ < 3.75$  and SExtractor F814W AB magnitude in the range 19–25. The nearly horizontal lines are the R.A. proper motions as a function of decl. expected in the Sangarius stream for either prograde (solid) or retrograde (dashed) orbits (Grillmair 2017). The red filled circles with error bars are the proper motions of two candidate Sangarius stream sources selected from their high space velocities in the Toomre diagram in Figure 17(b), listed in the first two rows of Table 3. The blue and green filled circles are the proper motions of 19 sources obtained from a color–magnitude diagram of metal-poor giant stars at the distance to the Sangarius stream. Of these, the green filled circles are three sources whose proper motions in both R.A. (panel (a)) and decl. (panel (b)) are consistent within two standard deviations with the expected motions in the Sangarius stream for either prograde or retrograde orbits (Grillmair 2017). (b) Same as panel (a) but for JSP proper motions in decl., also as a function of decl.

stars. In view of these caveats, these two stars are very questionable as candidates of Sangarius.

The proper motions of the candidates in the Sangarius stream and the possible substructure or stream E of it can be compared with the expected motions in the Sangarius stream. In Figures 19(a) and (b), we plot, respectively, the R.A. and decl. proper motions of all 10,818 empirical faint stars in our sample as a function of decl. Overplotted as red filled circles with error bars are the proper motions of the candidates listed in the first two rows of Table 3. Overplotted as blue and green filled circles are the proper motions of the candidates from the metal-poor color–magnitude diagram described above. The nearly horizontal lines are the expected proper motions in the Sangarius stream

(Grillmair 2017) for either prograde (solid line) or retrograde (dashed line) orbits.

It can be seen from Figure 19 that the two candidate sources that were selected from their high space velocities in the Toomre diagram of Figure 17 have motions consistent with those expected for prograde orbits in the Sangarius stream within one standard deviation. It can also be seen that, among the 19 sources selected from the metal-poor color–magnitude diagram for the Sangarius stream, three sources shown as green filled circles and listed in Table 3 under “Candidates from Color–Magnitude Diagram” have motions consistent within two standard deviations with those in this stream. Of these three sources, the first and third, as listed in Table 3, have R.A.

and decl. proper motions consistent with both prograde and retrograde orbits, while the second source has proper motions consistent with a retrograde orbit. The Galactic space velocities of these three stars at the distance of 20 kpc of the Sangarius stream are shown in Figure 17(b) as small red filled circles. It can be seen that these stars have high velocities, with two of them being candidate members of the halo and one of them being a candidate of the thick disk.

## 9. Conclusions

Astrometry obtained by jointly processing the HSC and ACS data sets has allowed us to measure proper motions of nearly six times more sources than Gaia DR2. We have been able to derive empirical parallaxes for these sources using ancillary Subaru Suprime-Cam photometry. The proper motions of late-type main-sequence stars at  $\sim 1$  kpc in the COSMOS field exhibit preferential motions (relative to the LSR) directed toward the Galactic center. We have identified candidate high-velocity stars, of which six are at relatively near distances to us,  $\sim 0.5$ – $6$  kpc, and five are candidate members of the  $\sim 20$  kpc distant Sangarius stream in the Galactic halo. The proper motions of the five Sangarius stream candidates are consistent with the motions previously observed in the stream, and it is possible that they are metal-poor objects that would be consistent with the halo environment. Spectroscopy of these sources is needed to confirm the above membership. We have also possibly identified a substructure or an additional stream parallel to Sangarius,  $\sim 1^\circ 8$  to the E of it.

We thank Dr. Davy Kirkpatrick for very insightful discussions and the anonymous referee for very helpful suggestions.

The Hyper Suprime-Cam (HSC) collaboration includes the astronomical communities of Japan and Taiwan and Princeton University. The HSC instrumentation and software were developed by the National Astronomical Observatory of Japan (NAOJ), the Kavli Institute for the Physics and Mathematics of the Universe (Kavli IPMU), the University of Tokyo, the High Energy Accelerator Research Organization (KEK), the Academia Sinica Institute for Astronomy and Astrophysics in Taiwan

(ASIAA), and Princeton University. Funding was contributed by the FIRST program from the Japanese Cabinet Office, the Ministry of Education, Culture, Sports, Science and Technology (MEXT), the Japan Society for the Promotion of Science (JSPS), the Japan Science and Technology Agency (JST), the Toray Science Foundation, NAOJ, Kavli IPMU, KEK, ASIAA, and Princeton University.

This paper makes use of software developed for the Large Synoptic Survey Telescope. We thank the LSST Project for making their code available as free software at <http://dm.lsst.org>.

Based in part on data collected at the Subaru Telescope and retrieved from the HSC data archive system, which is operated by the Subaru Telescope and the Astronomy Data Center at the National Astronomical Observatory of Japan.

This work has made use of data from the European Space Agency (ESA) mission Gaia (<https://www.cosmos.esa.int/gaia>), processed by the Gaia Data Processing and Analysis Consortium (DPAC; <https://www.cosmos.esa.int/web/gaia/dpac/consortium>). Funding for the DPAC has been provided by national institutions, in particular the institutions participating in the Gaia Multilateral Agreement.

This research used resources of the National Energy Research Scientific Computing Center, a DOE Office of Science User Facility supported by the Office of Science of the US Department of Energy under contract No. DE-AC02-05CH11231. This research is partially funded by the Joint Survey Processing effort at IPAC/Caltech through NASA grant NNN12AA01C.

*Facilities:* HST(ACS), Subaru(HSC), Gaia.

*Software:* SExtractor (Bertin & Arnouts 1996).

## Appendix A

### Description of Stellar Samples Used throughout This Paper

Various samples of stars, such as from Gaia, HSC, and ACS, are used throughout this paper. In order to clarify these samples, Table 4 briefly describes them and lists the number of stars contained in them and the initial section where they are mentioned.

**Table 4**  
Description of Samples of Stars in the COSMOS Field Used throughout This Paper

Number of Sources <sup>a</sup>	Description of Sample	Section in Paper	
2434	...	HSC–Gaia matches in all 133 HSC patches	3
...	1514	HSC–Gaia matches in the 63 HSC coadds common to ACS; subset of the above sample	3
1135	...	ACS–Gaia matches in the 63 ACS coadds	3
3937	...	Gaia–ACS matches unconstrained in apparent magnitude or parallax; 453 stars common to sample of 13,009 empirically selected stars	5
...	3386	Subset of the above; Subaru Suprime $r - i^+$ color in the range $-1.25$ to $3.75$ mag	7
...	3367	Gaia–ACS matches; positive Gaia parallax; subset of the above sample	7
...	2703	Gaia–ACS matches; positive Gaia parallaxes; Subaru Suprime $r - i^+$ color in the range $-1.25$ to $3.75$ mag; relative phot. uncertainties in $r$ and $i^+ < 0.2$ ; subset of the above	7
...	1010	HSC–ACS–Gaia matches fainter than $G$ of 18.5; Gaia parallax $> 0$ ; subset of the above sample of 3367 sources	4.1
...	972	HSC–ACS–Gaia matches fainter than $G$ of 18.5; Gaia parallax $> 0$ ; Gaia R.A. proper motions in the range $-30$ to $+20$ mas yr <sup>-1</sup> ; subset of the above sample	4.1
...	925	HSC–ACS–Gaia matches fainter than $G$ of 18.5; Gaia parallax $> 0$ ; Gaia decl. proper motions in the range $-20$ to $+10$ mas yr <sup>-1</sup> ; subset of the above sample of 1010 stars	4.1
...	148	Subset of the above sample of 1010 Gaia stars; Subaru Suprime $r - i^+$ colors in the range $2.75$ – $3.75$ for late-type main-sequence luminosity class	7
13,009	...	Empirically selected stars in ACS coadds of SExtractor F814W AB mag 19–26; includes 453 Gaia stars in the above sample of 3937 sources	5
...	11,519	Empirically selected stars HSC matched to ACS; SExtractor F814W AB mag in the range 19–25; excludes 264 Gaia stars that were common to the above sample of 1010 stars; subset of the above	7
...	10,818	Subset of the above; Subaru Suprime $r - i^+$ colors in the range $-1.25$ to $3.75$ mag relative phot. uncertainties in $r$ and $i^+ < 0.2$	7
...	10,816	Subset of the above; empirically derived main-sequence luminosity class	7
...	8358	Subset of the above; late-type main-sequence stars with Subaru Suprime $r - i^+$ colors in the range $2.75$ – $3.75$ mag	7
...	1540	Subset of the above; late-type main-sequence stars with SExtractor F814W AB mag in the range 24–25	7
12,529	...	Combination of the above samples of 11,519 empirically selected stars and 1010 Gaia stars	6.3

**Note.**

<sup>a</sup> The number of sources is listed in the second column of the table if the sample is a subset of another sample.

### Appendix B

#### Parallax and Total Proper Motion Relations for High-latitude Gaia DR2 Sources Distributed at Various Longitudes

Section 7 presented polynomial fits to the relations between Gaia DR2 parallax and total proper motion in samples of constrained  $r - i^+$  color and luminosity class. A limitation of the relations in Table 1 is that the total motion consists of only total proper motion or tangential velocity and does not include radial velocity. In order to assess the validity of our relations, we obtained the total proper motions and parallaxes of all Gaia DR2 stars with Galactic latitude  $b > 40^\circ$  and distributed at all Galactic longitudes. In this way, unknown radial velocities could be assumed to randomly span most possible values, and the extinction could be taken as low as that in the COSMOS field. As in Section 3, only single, nonvariable Gaia DR2 sources fainter than  $G = 18.5$  mag and with parallax  $> 0$  were considered. The spectral type of the sources was estimated from the Gaia color  $G_{BP} - G_{RP}$  in the Vega system after first generating synthetic  $G_{BP} - G_{RP}$  colors of main-sequence and giant stars by convolving empirical templates of stellar spectra (Kesseli et al. 2017) with the transmission functions of the  $G_{BP}$  and  $G_{RP}$  filters (Gaia Collaboration et al. 2016, 2018). The luminosity class (main sequence or giant) of each Gaia DR2 source was discriminated by comparing  $G$  with the apparent magnitude derived from the distance modulus for either main-sequence or giant stars, similar to Section 7.

These high-latitude Gaia DR2 stars were binned in representative groups for comparison of their parallax versus total proper motion relation to those groups in Table 1 of approximately similar spectral type and luminosity class ranges. The data sets from which the groups were drawn consisted of 729,514 stars with  $2.75 < G_{BP} - G_{RP} < 3.75$  or spectral type M5–M8, 3,810,892 stars with  $0.8 < G_{BP} - G_{RP} < 1.2$  or spectral type G4–K3, and 2,470,402 stars with  $1.2 < G_{BP} - G_{RP} < 1.5$  or spectral type K4–K7. Table 5 lists the representative bins of main-sequence and giant stars drawn from the above three data sets. These representative bins are each approximate supersets of the respective bins listed in Table 1.

Upon comparing Tables 1 and 5, it can be seen that the Gaia DR2 parallax versus proper motion relations of all high-latitude stars are “shallower” (have a smaller slope) than those of the COSMOS field. Figure 20 shows this relation for K4–K7 Gaia stars at all high latitudes for comparison with Figure 14 (M2–M3 Gaia stars in COSMOS). Figures 14 and 20 and Tables 1 and 5 show that the relation for all high-latitude stars is a factor of  $\sim 2$  shallower than that for the COSMOS field. The “zero-intercept” or zeroth-order coefficient of the fits is comparable to within  $\sim 20\%$ , which represents the most distant stars in these relations. We believe that the above comparison gives an idea of the uncertainty of these relations in the absence of radial velocity information.

We also compared the relations of parallax versus proper motion for some of the most distant stars, namely, giants of spectral types K8–M1 in either the COSMOS field or eight

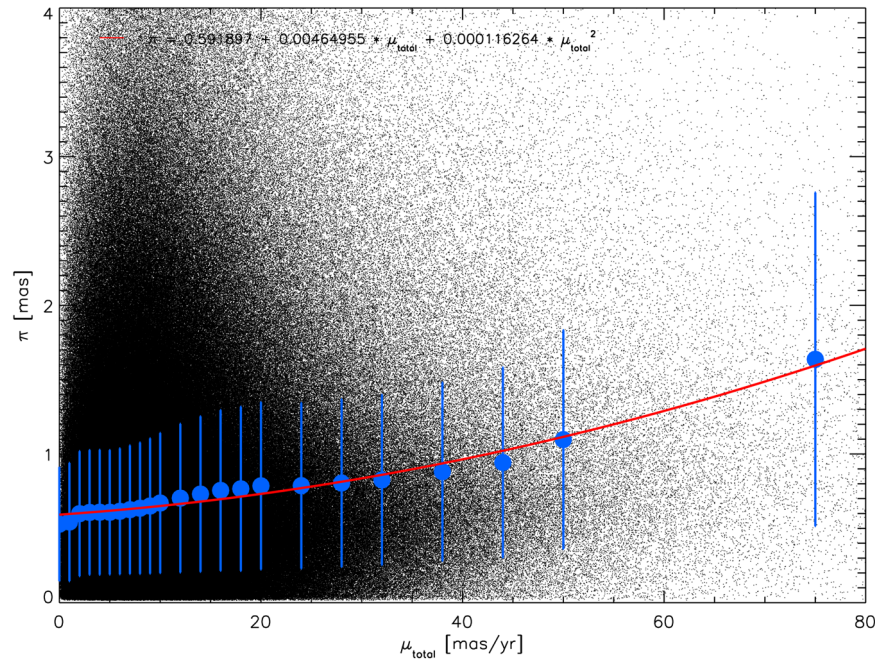


**Figure 20.** Gaia DR2 catalog parallax as a function of total proper motion for late K-type main-sequence Gaia DR2 stars (whose luminosity class and spectral type were determined as described in the text) with Gaia colors in the interval  $1.2 < G_{BP} - G_{RP} < 1.5$  and parallaxes  $>0$  indicating valid Gaia DR2 solutions. These sources were drawn from 2,470,402 stars at Galactic latitude  $b > 40^\circ$  and distributed at all Galactic longitudes. The small black symbols correspond to individual stars. The large blue symbols with error bars are the proper motion–binned means and standard deviations of parallax. The solid red line is a second-order polynomial fit to the proper motion–binned means.

**Table 5**

Polynomial Fits to the Relation of Gaia DR2 Parallax as a Function of Total Proper Motion, Color, and Luminosity Class for Representative Groups Drawn from All Gaia DR2 Stars at High Galactic Latitude<sup>a</sup>

Color $G_{BP} - G_{RP}$	Spectral Type	$a_0$	$a_1$	$a_2$	$a_3$
<b>Main-sequence Stars</b>					
0.80–1.20	G4–K3	$0.52 \pm 0.11$	$-0.017 \pm 0.018$	$6.7 \times 10^{-4} \pm 6.5 \times 10^{-4}$	$1.03 \times 10^{-5} \pm 5.9 \times 10^{-6}$
1.20–1.50	K4–K7	$0.592 \pm 0.016$	$0.0046 \pm 0.0014$	$1.16 \times 10^{-4} \pm 2.0 \times 10^{-5}$	...
2.75–3.75	M5–M8	$1.997 \pm 0.016$	$0.0225 \pm 0.0014$	$2.9 \times 10^{-4} \pm 2.0 \times 10^{-5}$	...
<b>Giant Stars</b>					
0.80–1.20	G4–K3	$0.01813 \pm 0.00021$	$-1.39 \times 10^{-4} \pm 4.5 \times 10^{-5}$	$6.2 \times 10^{-6} \pm 1.9 \times 10^{-6}$	...
1.20–1.50	K4–K7	$0.014929 \pm 0.00053$	$2.8 \times 10^{-5} \pm 2.4 \times 10^{-5}$	...	...
2.75–3.75	M5–M8	$0.02198 \pm 0.00038$	$8.68 \times 10^{-5} \pm 3.72 \times 10^{-5}$	...	...

**Note.**

<sup>a</sup> Polynomial fits to the relation of Gaia DR2 parallax as a function of total proper motion, also as a function of Gaia DR2 color  $G_{BP} - G_{RP}$  and luminosity class (main-sequence or giant stars). These relations were established from 729,514 stars with  $2.75 < G_{BP} - G_{RP} < 3.75$ , 3,810,892 stars with  $0.8 < G_{BP} - G_{RP} < 1.2$ , and 2,470,402 stars with  $1.2 < G_{BP} - G_{RP} < 1.5$ , all with a positive Gaia DR2 parallax. The polynomial fits are of the form  $\pi = a_0 + a_1\mu_{\text{total}} + a_2\mu_{\text{total}}^2 + a_3\mu_{\text{total}}^3$ , where it is implied that  $a_2$  and  $a_3$  are zero if not listed. The quoted errors in the polynomial fit coefficients are  $\pm 1$  standard deviation.

high-latitude fields. The latter were chosen to be  $1.64 \text{ deg}^2$  in size, analogous to the size of the COSMOS field covered by ACS, at Galactic latitudes  $b > 40^\circ$  (with one field at  $b < -40^\circ$ ) and equally distributed in Galactic longitude. Figure 21 shows the parallax versus total proper motion relations for these fields. The fit parameters of these fields are indicated in each panel in Figure 21, including for the COSMOS field giant stars in the upper left panel, and in Table 1 for the latter.

Figure 21 shows that the Gaia DR2 parallax uncertainties are very large for these distant sources. The linear fits are mostly flat for total proper motions up to  $15 \text{ mas yr}^{-1}$  in most cases, and there are generally few available sources in each field, although the fields at  $(l, b)$  of (357, 42) and (57, 42) have 32 and 20 sources, respectively. If radial velocities were available,

the slopes of the linear fits would be smaller in absolute value because all abscissae would be incremented. Thus, the slightly negative slopes in the fields at (297, 42), (117, 42), (357, 60), and (117, 60) are most likely due to the lack of radial velocities.

The resulting fits of the relations of Gaia parallax versus total proper motion for distant stars have very large uncertainties. For example, the linear fit parameters for the COSMOS field giants of K8–M1 type listed in Table 1 have relative uncertainties of  $\sim 380\%$  and  $33\%$  in the zero-intercept ( $a_0$ ) and slope ( $a_1$ ), respectively. In view of the large uncertainties of parallax, the model of distance as a reciprocal of a single value of parallax fails, and distance must be assessed statistically instead. For this purpose, we reevaluated the distance of the two giant stars listed in the

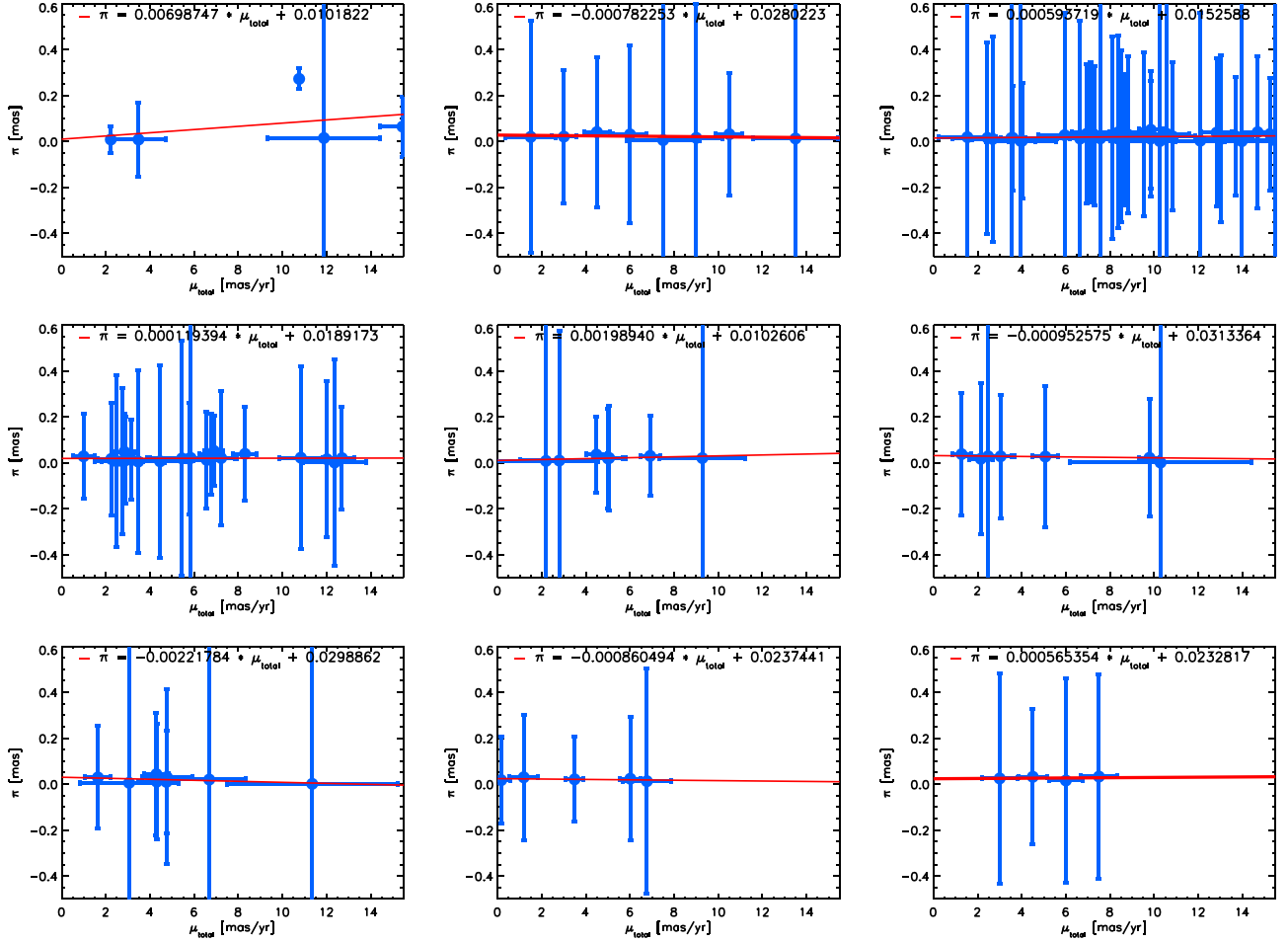


**Figure 21.** Gaia DR2 catalog parallax as a function of total proper motion for giant stars of type K8–M1 (whose luminosity class and spectral type were determined as described in the text) and with parallaxes  $>0$  indicating valid Gaia DR2 solutions. The upper left panel is for the five ACS–HSC–Gaia DR2 giant stars in the COSMOS field identified from the sample of stars with Subaru Suprime-Cam colors in the interval  $0.5 < r - i^+ < 0.8$ . The remaining panels are for Gaia DR2 stars in fields of  $1.64 \text{ deg}^2$  each, analogous to the COSMOS field but distributed at various locations at Galactic latitude  $b > 40^\circ$ . These stars were identified from a sample of sources with Gaia DR2 colors in the interval  $1.6 < G_{BP} - G_{RP} < 2.0$ . The blue filled circles with error bars correspond to individual stars, where the error bars are the Gaia DR2 catalog uncertainties. The solid red lines are linear fits to the data of the stars in each field. The panels, starting from the middle top and running from left to right and top to bottom, are for fields at Galactic longitude, latitude ( $l, b$ ) of (297, 42), (357, 42), (57, 42), (117, 42), (357, 60), (117, 60), and (57,  $-42$ ) in degrees. A field at (237, 60) had fewer than three giant stars and is omitted.

first two rows of Table 3. Given the uncertainties of Gaia DR2 proper motion and parallax and the uncertainties of JSP proper motion of these two sources listed in Table 3, we generated Gaussian deviations for these three parameters and calculated linear fits similar to that for K8–M1 giants in Table 1 and the upper left panel of Figure 21. Gaussian deviations that yielded a JSP parallax  $<0$  were discarded, and the Monte Carlo simulations were continued until 500

successful simulations were achieved. Figure 22 shows the histogram of the distances that were computed for the M0 III star. The median distance of the 500 simulations was taken as the distance to the source. The asymmetric lower and upper standard deviations were found at the distance values where the histogram contained 67% of the points below and above the median, respectively. These values are listed in the last column of Table 3 for these two stars.

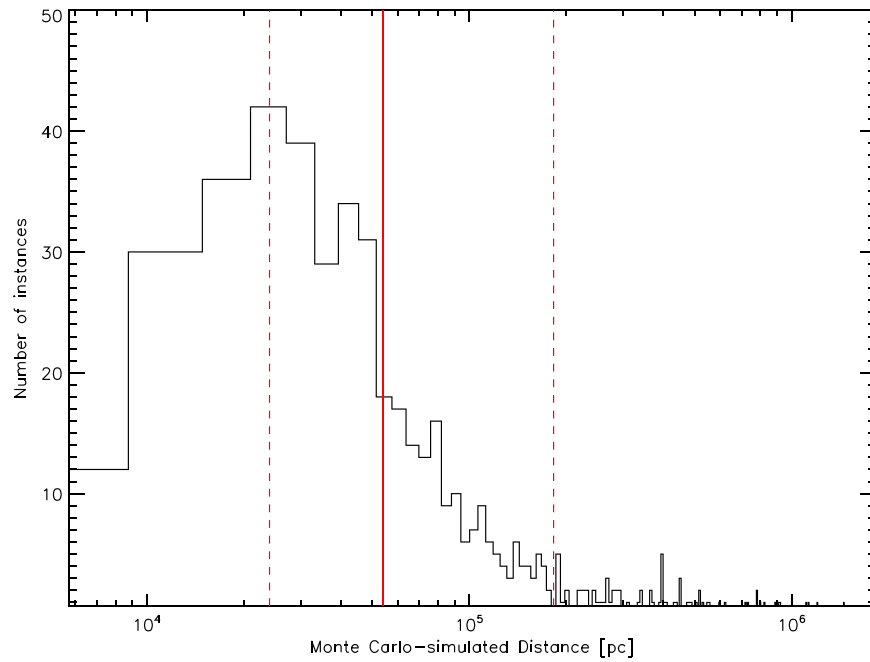


**Figure 22.** Monte Carlo simulation of distances for the giant star of spectral type M0 listed in the first row of Table 3. These distances are the result of generating 500 random Gaussian deviations to the Gaia proper motions and parallaxes of K8–M1 giant stars plotted in Figure 21 and the JSP proper motions of this star (Table 3). Linear fits were generated for each set of Gaia parallaxes and proper motions of the form listed in Table 1, and the JSP proper motions were applied in the linear fit to generate a parallax and, in turn, a distance. The solid red vertical line is the median distance, and the vertical dashed lines represent the  $\pm 66.67\%$  points of the distribution, corresponding to asymmetrical  $\pm 1\sigma$  (one standard deviation).

### Appendix C

#### High-velocity Stars Drawn from the Sample of Gaia–ACS Matches Distinct from Empirically Selected Stars

Section 5 indicated that our sample of stars with well-determined JSP proper motions, Subaru Suprime  $r - i^+$  colors in the range  $-1.25$  to  $3.75$  mag, and SExtractor F814W AB mag fainter than  $18.5$  consisted of 1010 Gaia DR2 sources matched to ACS and 10,818 empirically selected stars. The color range was established to exclude any abnormal stars, and the magnitude limit was meant to exclude saturated sources. In the sample of Gaia stars, which is distinct from the above sample of

empirically selected stars, and using the techniques described in Section 7, six stars were identified as having high Galactic space velocities (shown as statistical ranges of velocities by the dashed green lines in Figure 17). In Table 6, we list the observational data of these sources. These sources are inconsistent with membership in the Sangarius stream, which is 20 kpc from us. However, we list the sources as reference for any further observations. These stars are high-velocity candidates for which halo membership determination requires further follow-up, such as measurements of their metallicity. Alternatively, their high velocities might instead be due to gravitational encounters.

**Table 6**  
Candidate High-velocity Stars in the Gaia DR2 Proper-motion Sample

R.A. (J2000.0)	Decl. (J2000)	Gaia DR2 Proper Motions <sup>a</sup>		ACS F814W	Color $r - i^{+b}$	Spectral Type <sup>c</sup>	Luminosity Class <sup>c</sup>	Distance <sup>d</sup>
		$\mu_{\alpha}$ mas yr <sup>-1</sup>	$\mu_{\delta}$ mas yr <sup>-1</sup>					
h, m, s	d, m, s							kpc
09 57 59.04502	+02 42 39.6025	$-20.70 \pm 0.53$	$-1.54 \pm 0.38$	18.800	$+2.827 \pm 0.013$	Mid-to-late M	III	$2.43^{+3.7}_{-1.3}$
10 02 31.98050	+02 44 41.15652	$+22.59 \pm 0.81$	$-45.58 \pm 0.81$	18.855	$-0.3918 \pm 0.0042$	O8	V	$1.27^{+1.58}_{-0.57}$
10 01 11.28869	+02 47 42.95436	$-91.72 \pm 0.71$	$-23.44 \pm 0.75$	18.856	$-0.0542 \pm 0.0038$	A8	V	$0.93^{+0.65}_{-0.30}$
10 00 24.46502	+01 52 48.3867	$-16.81 \pm 0.52$	$-37.665 \pm 0.56$	18.874	$-0.4052 \pm 0.0036$	O4	V	$1.96^{+3.2}_{-0.92}$
09 59 11.15546	+02 00 46.6052	$+14.86 \pm 0.83$	$-36.17 \pm 0.72$	19.040	$+0.4832 \pm 0.0037$	K7	V	$2.0^{+3.9}_{-1.1}$
09 58 15.76378	+02 05 17.0138	$-62.86 \pm 1.02$	$-28.17 \pm 1.02$	19.236	$+0.1366 \pm 0.0052$	G3	V	$0.76^{+1.25}_{-0.28}$

**Notes.**

<sup>a</sup> Proper motions are from the Gaia DR2 catalog, corrected for the effect of solar motion, as explained in Section 7.

<sup>b</sup> Colors are from the Subaru Suprime-Cam COSMOS2015 survey (Laigle et al. 2016).

<sup>c</sup> Spectral types were derived from the synthetic colors of main-sequence and giant stars using models from Kesseli et al. (2017), as explained in Section 7. Luminosity class was inferred from the observed SExtractor F814W AB magnitude and absolute magnitudes of main-sequence and giant stars (see references in Section 7).

<sup>d</sup> Sources are from the sample of 1010 Gaia–ACS matched stars with Subaru Suprime  $r - i^{+}$  colors in the range  $-1.25$  to  $3.75$ , SExtractor F814W AB mag  $> 18.5$ , and positive Gaia parallaxes. In view of the large relative uncertainties of Gaia DR2 parallaxes for these sources, Monte Carlo simulations of parallax were carried out to derive asymmetric distributions of simulated distance, analogous to the simulations in Appendix B; see also Luri et al. (2018).

## ORCID iDs

Sergio B. Fajardo-Acosta  <https://orcid.org/0000-0001-9309-0102>  
 Andreas Faisst  <https://orcid.org/0000-0002-9382-9832>  
 Carl J. Grillmair  <https://orcid.org/0000-0003-4072-169X>  
 Ranga-Ram Chary  <https://orcid.org/0000-0001-7583-0621>  
 Roberta Paladini  <https://orcid.org/0000-0002-5158-243X>  
 Ben Rusholme  <https://orcid.org/0000-0001-7648-4142>  
 Nathaniel Stickley  <https://orcid.org/0000-0003-0987-5738>

## References

- Aihara, H., Armstrong, R., Bickerton, S., et al. 2018, *PASJ*, 70, S8  
 Bertin, E., & Armouts, S. 1996, *A&AS*, 117, 393  
 Civano, F., Marchesi, S., Comastri, A., et al. 2016, *ApJ*, 819, 62  
 Dotter, A., Chaboyer, B., Jevremović, D., et al. 2008, *ApJS*, 178, 89  
 Faisst, A. L., Chary, R. R., Fajardo-Acosta, S., et al. 2022, *ApJ*, 929, 66  
 Filippenko, A. V. 1982, *PASP*, 94, 715  
 Gaia Collaboration, Prusti, T., de Bruijne, J. H. J., et al. 2016, *A&A*, 595, A1  
 Gaia Collaboration, Brown, A. G. A., Vallenari, A., et al. 2018, *A&A*, 616, A1  
 Grillmair, C. J. 2006, *ApJL*, 651, L29  
 Grillmair, C. J. 2017, *ApJ*, 834, 98  
 Ivezić, Ž., Kahn, S. M., Tyson, J. A., et al. 2019, *ApJ*, 873, 111  
 Johnson, D. R. H., & Soderblom, D. R. 1987, *AJ*, 93, 864  
 Keenan, P. C., & Pitts, R. E. 1985, *PASP*, 97, 297  
 Kesseli, A. Y., West, A. A., Veyette, M., et al. 2017, *ApJS*, 230, 16  
 Koekemoer, A. M., Ausser, H., Calzetti, D., et al. 2007, *ApJS*, 172, 196  
 Kposov, S. E., Belokurov, V., Li, T. S., et al. 2019, *MNRAS*, 485, 4726  
 Laigle, C., McCracken, H. J., Ilbert, O., et al. 2016, *ApJS*, 224, 24  
 Lejeune, T., Cuisinier, F., & Buser, R. 1997, *A&AS*, 125, 229  
 Luri, X., Brown, A. G. A., Sarro, L. M., et al. 2018, *A&A*, 616, A9  
 Marchesi, S., Civano, F., Elvis, M., et al. 2016, *ApJ*, 817, 34  
 Martins, F., Schaerer, D., & Hillier, D. J. 2005, *A&A*, 436, 1049  
 Mihalas, D., & Binney, J. 1981, *Galactic Astronomy. Structure and Kinematics* (2nd ed.; San Francisco, CA: Freeman)  
 Mikami, T., & Heck, A. 1982, *PASJ*, 34, 529  
 Miyazaki, S., Komiyama, Y., Kawanomoto, S., et al. 2018, *PASJ*, 70, S1  
 Nissen, P. E. 2004, in *Origin and Evolution of the Elements*, ed. A. McWilliam & M. Rauch (Cambridge: Cambridge Univ. Press), 154  
 Oke, J. B. 1974, *ApJS*, 27, 21  
 Pecaut, M. J., & Mamajek, E. E. 2013, *ApJS*, 208, 9  
 Qiu, T., Wang, W., Takada, M., et al. 2021, *MNRAS*, 501, 5149  
 Scoville, N., Ausser, H., Brusa, M., et al. 2007, *ApJS*, 172, 1  
 Taniguchi, Y., Scoville, N., Murayama, T., et al. 2007, *ApJS*, 172, 9  
 Taniguchi, Y., Kajisawa, M., Kobayashi, M. A. R., et al. 2015, *PASJ*, 67, 104  
 Toomre, A. 1964, *ApJ*, 139, 1217  
 Venn, K. A., Irwin, M., Shetrone, M. D., et al. 2004, *AJ*, 128, 1177  
 Yan, Y., Du, C., Li, H., et al. 2020, *ApJ*, 903, 131  
 York, D. G., Adelman, J., Anderson, J. E. J., et al. 2000, *AJ*, 120, 1579